To the Graduate Council:

I am submitting herewith a dissertation written by Sirikul Sriprisan entitled "An Improved Knockout-Ablation-Coalescence Model for Prediction of Secondary Neutron and Light-ion Production in Cosmic Ray Interactions." I have examined the final electronic copy of this dissertation for form and content and recommend that it be accepted in partial fulfillment of the requirement for the degree of Doctor of Philosophy with a major in Nuclear Engineering.

Lawrence W. Townsend, Major Professor

We have read this dissertation
And recommend its acceptance:
Laurence F. Miller

Ronald E. Pevey

Thomas Handler

Accepted for the Council:
Carolyn R. Hodges, Vice Provost and Dean
of the Graduate School

(Original signatures are on file with official student records.)

AN IMPROVED KNOCKOUT-ABLATION-COALESCENCE MODEL FOR PREDICTION OF SECONDARY NEUTRON AND LIGHT-ION PRODUCTION IN COSMIC RAY INTERACTIONS

A dissertation
Submitted as a part of fulfillment for the Doctor of Philosophy Degree,
Nuclear Engineering,
The University of Tennessee, Knoxville, TN

Sirikul Sriprisan

August 2008

DEDICATION

For my mother and her unconditional love

and my Arnaud and his big heart.

Love you all.

ACKNOWLEDGEMENTS

Success does not come easy especially for my work and I could not accomplish it without the constant patience and full support from my wonderful advisor, Dr. Lawrence W. Townsend. I very much appreciate his excellent guidance in both research work and life in general. I furthermore would like to express my deep thanks to the members of my dissertation committee: Dr. Ronald Pevey and Dr. Laurence F. Miller from the Nuclear Engineering Department and Dr. Thomas Handler from the Physics Department for their helpful suggestions, guidance and commitment to help me accomplish my dissertation work.

Many thanks go to all my professors whose knowledge enable me to think and learn to become a capable engineer. Special thanks also go to staff members in the Nuclear Engineering Department at UT, especially Kristen England and Gary Graves for their constant help along the way and to the Nuclear Engineering Department at UT under the leadership of Dr. Lee Dodds for the support throughout my PhD studies. I also would like to express my appreciation to the National Aeronautics and Space Administration for their constant financial support of my research work. I furthermore would like to thank Dr. Thomas M. Miller, Oak Ridge National Laboratory, Dr. Lawrence H. Heilbronn (soon to join the faculty in UTNE), and the brand new doctoral graduate, Dr. Matthew W. Francis, for their insightful comments and suggestions, personally and professionally.

My special thanks also go to my good friends, Bob and Lynda Schnekerburger. Their friendships mean a lot to me. Thank you for the pep talk. I would have not been here today if it was not for unconditional love and support from my mom, Jim and Pat. Thanks a million and I love you mom. Lastly my deeply appreciation goes to a very special person in my life, my husband Arnaud whose patient love enabled me to complete this work.

ABSTRACT

An analytical knockout-ablation-coalescence model capable of making quantitative predictions of the neutron and light-ion spectra from high-energy nucleon-nucleus and nucleus-nucleus collisions is being developed for use in space radiation protection studies. The FORTRAN computer code that implements this model is called UBERNSPEC. The knockout or abrasion stage of the model is based on Glauber multiple scattering theory. The ablation part of the model uses the classical evaporation model of Weisskopf-Ewing. In earlier work, the knockout-ablation model was extended to incorporate important coalescence effects into the formalism. Recently, the coalescence model was reformulated in UBERNSPEC and alpha coalescence incorporated. In addition, the ability to predict light ion spectra with the coalescence model was added. Earlier versions of UBERNSPEC were limited to nuclei with mass numbers less than 68. In this work, the UBERNSPEC code has been extended to include heavy charged particles with mass numbers as large as 238. Representative predictions from the code are compared with published measurements of neutron energy and angular production spectra and light ion energy spectra for a variety of collision pairs.

TABLE OF CONTENTS

LIST OF FIGURES

SYMBOLS AND DESCRIPTIONS

A	mass number
B	two-body slope parameter, fm^2
b	impact parameter, fm
c	speed of light, m/sec
E	energy, MeV
F	fragment
F^*	prefragment
F_l	probability of emission of ion l
f	scattering operator, fm
g_n	statistical weight
Im	imaginary part of function
$J_m^{(1)}$	cylindrical Bessel function of first kind of order m
K	projectile target relative wave number, fm^{-1}
k	wave number of emitted neutrons, fm^{-3}
M	mass, MeV/c^2
m_N	nucleon mass, MeV/c^2
N_1	single-collision term
n	number of abraded nucleons
$n(\mathbf{p})$	momentum distribution
$n(\mathbf{x})$	Fourier transform of nucleon momentum distributions
P	projectile
$p(\mathbf{b}, \mathbf{b}')$	function describing projectile spectators
Q	$Q = \prod_{\zeta=1}^{A_T} (1 - \Gamma_{\zeta,j})$
T	target
w_0	level density of residual nucleus
X	final target state

r	internal nuclear coordinate, fm^3
z	component of **r**
s	transverse part of **r**
S_n	separation energy, MeV
ħ**q**	momentum transfer, fm^{-3}
α	ratio of real to imaginary parts of f_{NN}
β	relative projectile target velocity
Γ	profile function
δ(x)	Dirac delta function
ζ	target constituent
μ_n	neutron mass
ξ	defined in equation (27)
Λ_n	defined in equation (26)
ρ(**r**)	one-body density, fm^{-3}
ρ(r, r′)	one-body density matrix, fm^{-3}
σ	cross section, mb
φ(**r**)	single-particle wave function
c	velocity of light (m/s)
χ	Eikonal phase
Ψ	complete nuclear wave function
Ω	Eikonal inelastic collision term
abl	ablation
abr	abrasion
ko	knockout
CN	compound nucleus formation
f	final state
i	initial state
j	abraded nucleons (projectile constituents)
NN	nucleon-nucleon (two-body)
X	unobserved final target state

1. INTRODUCTION

A new vision for space exploration in the 21st Century includes extending human exploration to the Moon, Mars and beyond the Earth's orbit for scientific discovery, and it leads to a new focus on long duration, deep space missions. To accomplish these missions, the safety of the crews needs to be addressed. The natural space environment is dominated by high-energy heavy-charged (HZE) particles, which are a major source of radiation dose to human crews and electronic components in a spacecraft. Studies also show that some of the secondary particles can penetrate the Earth's atmosphere. These doses are a possible health risk to airplane crews and passengers on high attitude long-distance flights [2; 51; 81; 122]. The most probable cause of mortality from chronic exposure in space missions is the induction of late-occurring cancers. Other health risks include cataract formation and the possibility of damage to the central nervous system [81]. Although the radiobiological risks from these HZE particles are the subject of numerous experimental and theoretical investigations, the actual risks are essentially unknown as a result of the complexity of the space environment containing various type of particles, energies and amount of radiations from these particles, and the lack of human exposure data for many of these particle types and energies [81; 90; 103]. To establish protection from these high-energy radiations during long-term space exploration, accurate and precise radiation transport models and efficient and effective shielding designs are required. To accomplish this goal, the development of appropriate nuclear databases for the transport models used for space radiation shielding design is necessary.

The main goal of this present study is to provide a reliable database of relevant nuclear cross sections to use in the radiation transport model calculations. The methods of generating the nuclear databases for secondary particle productions from HZE transport are often obtained from semi-empirical formulations and theoretical models. In this work the fundamental physics for the secondary particle production modeling is described by a fragmentation theory based upon the abrasion-ablation process. This two-stage process incorporates the simple idea that the interaction between two relativistic heavy particles, projectile *P* and target *T,* can be visualized as the projectile *P* moving at initial momentum ***p*** colliding with the stationary target T, and the overlapping portions of their nuclear volumes are then sheared off by the collision [10; 67; 68; 82] as illustrated in Figure 1.1 (re-illustrated from Giacomelli et al. [54]). This is the abrasion (or knock out) process. The remaining piece of projectile or target, called a prefragment or spectator, continues on its initial trajectory with its pre-collision velocity. The final state of both the projectile and target nucleus is reached when the excited prefragments decay by emitting gamma rays and/or they disintegrate into fragments and nucleons. This process is known as ablation. The production cross sections of these nuclear fragments and isotopes are needed as an input into the radiation transport code in order to properly describe the transmitted radiation fields.

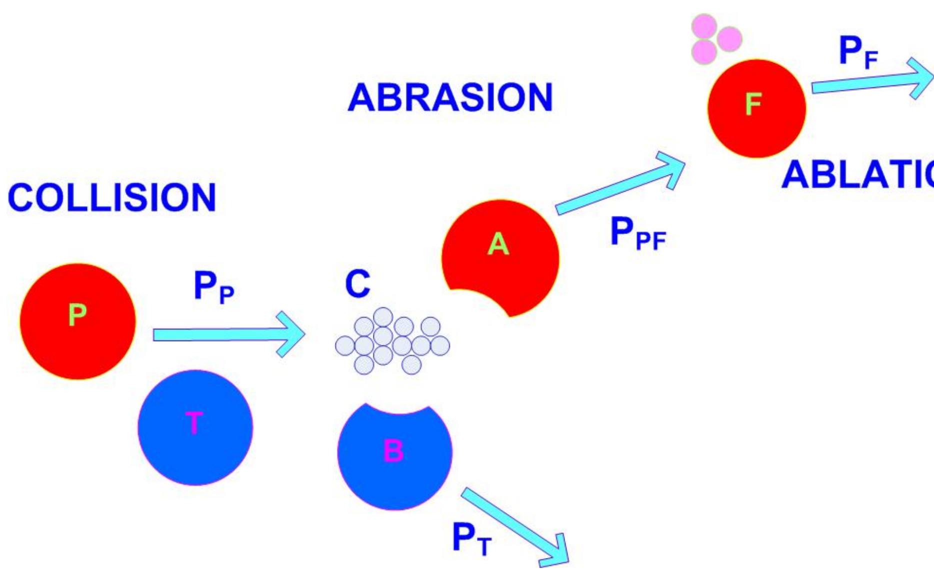

Figure 1.1: Schematic of the abrasion-ablation reaction and corresponding momentum at each step according to the fire-ball model [10]. The two-step reaction is illustrated as the projectile P colliding with the target T. As a result, the system partitions into 3 parts: projectile spectator A (prefragment), target spectator B, and participant C. This is the abrasion or knockout process. The prefragment is then de-excited and decays to the ground state; this process is known as ablation. The figure is adapted from Giacomelli et al. [54].

This work is based on extending the theoretical abrasion-ablation model presented in Cucinotta et al. [26] for predicting secondary neutron production from HZE particle collisions. Braley et al. [11] initially extended this abrasion-ablation model by incorporating the coalescence effects into the formalism to predict the loss of neutrons through production of light ions. Light ion production in these nuclear collisions was first introduced by Butler and Pearson [13], who calculated the production of deuterons from the high-energy proton collisions. Awes et al. [1] presented theoretical coalescence effects and the measurements of energetic *protons* ^{1}H*(p)*, *deuterons* ^{2}H(*d*), *tritons* ^{2}He(*t*), *helions* ^{3}He(*h*) and *alphas* ^{4}He(α). The fundamental assumption of the coalescence model is that two nucleons whose relative momentum is small and which are physically close together coalesce to form particles such as the light particles ($A \leq 4$) previously mentioned.

Currently there are a few nuclear fragmentation cross section models and limited nuclear fragmentation databases that can be adequately used for radiation assessment and shielding from the high-energy heavy-ions in the space radiation environment. One of these nuclear models is the NUCFRG2 code [117], which has been used widely to construct nuclear fragment databases at high energy, and incorporated into the high-energy heavy-fragment transport codes such as HZETRN [28; 92] and HETC-HEDS [76]. The basic physics for the NUCFRG2 code follows the geometric overlap approach by Bowman et al. [10] to describe the abrasion-ablation process with some additional approximations and corrections included in the model. Another nuclear model is the QMSFRG code which was developed by Cucinotta and collaborators [29] based on the quantum mechanical optical approach of Glauber multiple-scattering theory. The main focus of the QMSFRG code is the ability to calculate light-ion production cross sections by incorporating coalescence effects. Note that the underlying physics of the UBERNSPEC and the QMSFRG codes are similar.

To achieve the goal of developing an accurate and reliable nuclear fragmentation cross section model for HZE particle interactions, improvements of the previous abrasion-ablation-coalescence version are required. These modifications, which are the main focus in this work, include

A. Reformulating of the coalescence model in the UBERNSPEC code to predict light ion spectra
B. Extending the coalescence model to include the contributions from α production
C. Extending the code to handle mass numbers greater than 68
D. Expanding the coalescence calculations to other p_0 (coalescence radii in momentum space) values
E. Correcting significant existing coding errors in transforming between various reference frames

As described in subsequent sections, validation of the calculations obtained from UBERNSPEC is made by comparisons of predicted and measured nuclear fragmentation cross sections.

The remaining chapters in this report are divided as follows: Chapter 2 describes the fundamental formalism of the knockout-ablation-coalescence model including the literature review; Chapter 3 discusses previous work on UBERNSPEC presented in Cucinotta et al. [26] and in Braley et al. [11]; Chapter 4 presents a description of the current UBERNSPEC code and its modifications ; Chapter 5 displays sample results and comparisons with experimental data; and Chapter 6 is conclusions and suggestions for future work. Lastly, the list of references and appendices are presented, including detailed coding in the UBERNSPEC program.

2. KNOCKOUT-ABLATION-COALESCENCE FORMALISM

2.1. Literature review

The scattering of high-energy heavy-ion particles has been described using a variety of concepts. One of the successful approaches is the abrasion-ablation model, which has been discussed in detail in several of the references [10; 67; 68; 82; 98]. In the abrasion-ablation process, two relativistic heavy ions (the projectile and target nuclei) collide with each other resulting in an overlap of their nuclear volumes which are suddenly sheared away by the collision. The nuclei are assumed to have sharp spherical surfaces. The projectile is assumed to travel in a straight-line trajectory [82; 99] with its pre-collision velocity after the collision, whereas the target is assumed to be stationary. The process by which the overlapping nuclear portions are sheared away by the collision is known as the abrasion or knockout process. Nucleons from the projectile and target interacting in the geometrical overlap zone are therefore called participants; the other nuclear fragments outside the interaction zone are known as spectators [68]. After the collision, the participants and spectators (prefragments) decay by emitting gamma rays and/or other nuclear particles. This is the ablation process.

In the abrasion stage of the collision, cross sections can be modeled by two different formalisms: (1) using the classical geometric overlap model [10; 60; 82], and (2) using expressions based on the Glauber multiple-scattering theory [8; 67]. In the classical geometric overlap model, the physical concept is simple: the colliding nuclei are treated classically as spheres with uniform densities, sharp surfaces, and straight-line trajectories [99]. The number of abraded nucleons is related to the volume of the overlapping regions. Using the concept of the liquid drop model for the nucleus, the cross sections of abraded nuclei are given by [10; 82]

$$\sigma_{abr}(A_{PF}) = \pi[\mathbf{b}(A_{PF}+0.5)^2 - \mathbf{b}(A_{PF}-0.5)^2] \qquad (1)$$

where $\mathbf{b}$ is the abrasion impact parameter and A_{PF} is the prefragment mass number; A_{PF} =

$A_p - n$, where A_p is the projectile mass numbers and n is the number of abraded nucleons. The basic assumptions of this geometric abrasion model are that there is no energy dependence in any variables and the neglect of the diffuse nuclear surface [99].

The alternative (and more complex) abrasion-ablation model is based on the Glauber multiple-scattering theory. Unlike the classical geometric overlap model, the Glauber multiple-scattering model uses a quantum mechanical formulation based upon an optical limit potential approximation to the nucleus-nucleus multiple-scattering series [98]. The formalism is fully energy dependent, uses realistic nuclear density distributions, and includes the finite nuclear force effects for a nucleon-nucleon interaction [98]. In the multiple-scattering series with optical potential approximation, the cross section produced by the abrasion process is

$$\sigma_{abr}(A_{PF}) = \binom{A_P}{n} \int d^2\mathbf{b} [1 - P(\mathbf{b})]^n P(\mathbf{b})^{A_{PF}} \tag{2}$$

where

$$P(\mathbf{b}) = \exp[- A_T\, \sigma(e) I(\mathbf{b})] \tag{3}$$

and

$$I(\mathbf{b}) = [2\pi B(e)]^{-3/2} \int d z_0 \int d^3\xi_T \rho_T(\xi_T) \int d^3\mathbf{y} \rho_P(\mathbf{b} + z_0 + y + \xi_T) \exp\left[-\frac{y^2}{2B(e)}\right]. \tag{4}$$

The variable e is defined as the nucleon-nucleon kinetic energy in their center of mass frame, z_0 is the target center of mass position in the projectile rest frame, ξ_T represents target nucleus internal coordinates, and y is the projectile-target nucleon relative coordinates. The parameters: $\sigma(e)$ (the nucleon-nucleon cross section) and $B(e)$ (the nucleon-nucleon elastic scattering slope parameter) were obtained from compilations [3].

In the following subsection, a broad literature review involving the development of this alternative abrasion-ablation model using the Glauber multiple-scattering approach is described. The investigation of the high-energy heavy-ion multiple scattering interaction process began as a part of a nuclear structure study [50], based on the simplest nucleon-deuteron collision process, including the effects of both single and double scattering [42]. Numerous theoretical approximations for treating high-energy collisions have been presented in the literature, but for this review, the only focus is the Glauber theoretical analysis, which was first developed for predicting total cross sections for high-energy collisions of nucleons and π mesons with deuterons, based on the assumption that the single scattering of the neutron and proton in the deuteron after the collision with incident nucleons or mesons can be treated as independent events using the generalized diffraction method [55]. In the later seminal paper "High-Energy Collision Theory" by Glauber [56], the mathematically comprehensive theory began with a discussion of a general and simple single elastic scattering problem, and then developed into the high-energy applications. Unlike the previous approach, the "High-Engergy Collision Theory" work [56] involved the use of an empirical optical limit approach, which depends on the fluctuations and correlations of the individual nucleons. The main difference between these two methods is that the former method (also known as the full Glauber multiple-scattering series) is generally limited to use with a light particle ($A \leq 4$) for either or both the projectile and target and is tediously time consuming [46]. The later method is simpler and yields a general means for calculating cross sections from complex scattering processes [47].

The extension of the optical potential method in Glauber multiple-scattering theory has appeared in a number of studies [33; 34; 42; 43; 44; 48; 63] in terms of correlations and corrections to the usual optical limit approach, which is widely known for describing hardron-nucleon scattering collisions. The extension of the optical model approach by Franco [42] involved reformulations of the theoretical analysis to be more general and accurate by incorporating an Eikonal diffraction approximation (or single- or double-scattering treatments [59]) to predict the differential cross section for double scattering and the effects of spin-independent interactions. Similar work was also presented by Harrington [63]. Another study by Franco and Glauber [43] presented an improvement of the generalized Glauber theoretical analysis by accounting for the contributions of various cross-section correlations such as single and double scattering and their interference terms. The authors showed that for high-energy proton-deuteron elastic collisions the double scattering collision becomes the dominant process at scattering away from the forward direction. Subsequent work presented by Czyż and Maximon

[33] involved a generalized formulation of the elastic scattering amplitude at small scattering angles for composite particles. The calculation of elastic scattering using matter densities of the composite units was constructed. The resultant comparisons with the measured data showed that a more refined version of the multiple-scattering approach (which would account for large scattering angles) was needed in order to improve the calculations. At the end, the authors discussed briefly the use of the optical potential model versus the classical optical limit approach in Glauber theory, and the improved version showed a better fit with the experimental data. Harrington [64] indicated that the cancellation of the off-shell corrections by the higher order terms in the multiple-scattering expansion is necessary for the validity of the Glauber theory in the high-energy small-angle optical potential method with two-body interactions. The author demonstrated how the cancellation can be done and also developed the expressions in term of the off-shell two-particle *t* matrices, the Green's functions and time dependent operator using the Eikonal approximation. Similar work was also presented in Osborn [83]; both studies from Harrington [64] and Osborn [83] stated that the Glauber theoretical analysis yields exact, not an approximate solution, and the corrections of this approach are necessary to obtain accurate predictions. In work presented by Osborn [83], Glauber theory was obtained without the Eikonal approximation and the new formalism was derived from the unitarized impulse approximation outside of the Eikonal scattering predictions. More details of a unitarized impulse treatment are presented in later subsections.

Due to two important limitations: the elastic scattering divergence of momentum transfer as nuclear mass becomes larger, and the lack of the additional correlation for treating the spreading of the center-of-mass wave function [48], further studies to improve the optical limit into a more general approach were developed. Franco [45] presented very simple and useful analytical expressions for treating heavy-ion elastic scattering at high energy with Coulomb effects included. The results were accurate only at small momentum transfers since the point charge approximation for Coulomb scattering nuclei is not valid at large momentum transfer and leads to divergence at the end. In the sequent study [46], the author developed the numerical analysis using previously presented expressions for any given nucleon in either projectile or target to undergo multiple-scattering collisions.

This approach later known as the optical phase shift potential approach works well for predicting total cross sections and fragmentation cross sections for nucleus-nucleus scattering. The construction of the exact optical phase shift function was presented in Franco and Tekou [48]. It is showed that the use of this modified approach leads to significant improvement in the nucleus-nucleus total cross sections and elastic scattering differential cross sections and reduction of the divergence problem at large momentum transfers. The work by Franco and Nutt [47] and [50] also illustrated the effects of Pauli correlations in the expansion of the optical phase shift potential approximation. The authors concluded that the inclusion of the short-range correlations is necessary to reduce the problem presented in the classical optical limit approach such as divergence of elastic scattering at large momentum transfer and the addition of the center-of-mass correlations.

Up to now, the works discussed involve corrections and extensions of the usual optical model to the new optical phase shift approach and successfully applying this model to Glauber multiple-scattering theory. In the following subsections a few attempts to develop simple, yet general high-energy heavy-ion multiple-scattering interactions using an impulse approximation approach are described [15; 16; 17; 40; 41; 59; 69; 71; 86; 105]. The basic idea of impulse approximation was introduced by Chew [15] in an attempt to explain the high-energy elastic scattering process for neutron and deuteron total cross sections using an alternative method other than the Born approximation. The fundamental assumptions underlying the approximation are the following: (1) There is only a single interaction of the incident particle with a target nucleon at a time, (2) The amplitude of the incident wave stays nearly the same as if it is alone; and (3) The effect of the binding force during the strong collision phase is negligible [16; 17]. As a result, the explicit formula for the double scattering process was presented. However, Watson [105] mentioned that these treatments appear to be too complicated for describing a systematic multiple-scattering problem and for a derivation of the optical models. The approximation introduced by Watson [105] involves a separation of the coherent and the incoherent effects in the solution to the Schrödinger equation (assuming a large number of scattering nucleons) and the systematic corrections to the model appear to be quite straightforward. The author, however, concluded that the use of the optical potential model for nucleon-nucleon interactions is difficult and needed further study due to the lack of detailed knowledge of the two-nucleon interaction process. A few years later, very detailed studies [14; 94] introduced both experimental and theoretical expressions for nucleon-nucleon (especially proton-proton) scattering amplitudes at high energy. Further work by Bethe [6] demonstrated a success in using these nucleon-nucleon scattering amplitude expressions to predict the forward angular elastic distribution. This theoretical analysis of the nucleon-nucleon scattering amplitude was re-examined, and the optical model potential was derived, based on the two nucleon scattering amplitude by Kerman et al. [69]. The model includes the Coulomb potential of the nuclear charge distributions, ignores the interference between the amplitudes at each individual collision, and expresses as the exact *S*-matrix scattering series operator. Feshbach and Hüfner [39] reported that the series of the optical model potential by Kerman et al. [69] contains highly complicated phases as it depends on the dynamic structures of both projectile and target nuclei. The first term in the scattering series, according to the authors, represents scattering events expressed in terms of a single-particle density of the target nucleus. The second term is similar to two-body correlation functions. The work by Feshbach and Hufner [39], furthermore, focused on the explanation and validation of these correlations for numerical calculations, and derived the relation between the generalized semiclassical coupled solutions using the optical potential scattering and the Glauber expressions for the multiple-scattering process.

The connection between the Glauber multiple-scattering approximation theory and the Watson impulse approximation was presented in several studies. Osborn [83] showed that the fundamental physical properties of the Glauber addition formalism not only resolve the exact three-body Eikonal scattering problem and are unitary, but also include the impulse approximation and the shadow scattering effects. (The shadow scattering effect is defined as a well-defined shadow of the incident nucleon causing the double scattering effects by the other nucleon to be reduced as the longitudinal distance increases to infinity [55].) The author referred to the works by Pumplin [85] and Bhasin and Verma [7], which claimed that the Glauber theory is a truncated form of the Watson multiple-scattering theory. Pumplin [85], furthermore, presented a formulation of the corrections for the small-momentum drawback at high energy by including the higher-order multiple-scattering terms. Similar expressions were described by Remler [87]. Expansions of the Pumplin and Remler approximation were developed by Wilson [109]; as a result, a simple but accurate form of two-body elastic double scattering amplitude including both projectile and target recoil motion was demonstrated that is applicable at all momentum transfers. The approximated amplitudes were evaluated explicitly within the context of a Gaussian model. Subsequent work, also by Wilson [110], focused on an extended expression for the optical potential operator and evaluated the new multiple-scattering series for composite systems. The new and more accurate exact multiple-scattering amplitude series including all target recoil terms and neglecting two-body scattering assumptions was developed and appeared to be a natural extension of the Watson impulse formalism. The new optical potential model showed advantages over the classical model as: (1) The exact scattering series converged quickly at large momentum transfer [96], and (2) The approximation yields to more accurate predictions even for high-energy heavy-ion scattering and for light-ion collisions [114].

This review cannot be complete without a discussion of the works that involved the development of the abrasion (knockout)-ablation theory. As described at the beginning of this review, the abrasion-ablation model was developed based on two different processes: the classical geometric overlap and the Glauber multiple-scattering models. It is believed that the model was first described by Bowman and collaborators [67]. The work by Hüfner et al. [67], which is used as a physical basis for this analysis, involves the derivations of general expressions for calculating abrasion-ablation cross sections within the Glauber multiple-scattering theory. In the Hüfner approach, the abrasion was treated as an inelastic scattering process and a few simple approximations including the optical phase shift model and the coherent formalism were used to derive the abrasion cross section expression. Furthermore, frictional spectator interaction (FSI) effects (caused when a participant nucleon scatters through the remaining fragment matter of a spectator depositing additional energy before it leaves the nucleus) were included to improve the calculations of the fragmentation cross sections. The authors concluded that the abrasion-ablation-FSI model provides satisfactory prediction results for the fragmentation cross section in high-energy heavy-ion reactions. Further development by Oliveira et al. [82] used the abrasion-ablation model of Bowman et al. [10] with the clean-cut fireball model [107] for developing the abrasion stage. In the ablation process, the focus was on following projectile and target spectator fragments to the end. The preliminary comparisons of this unmodified abrasion-ablation model with experimental data showed the need to include additional surface energy depositions into the ablation process in order to reduce the overestimated production cross sections. The authors then presented a computational model, which included the FSI mechanism, and the resultant comparisons between the theoretical and experimental data were significantly improved.

Clearly, high-energy heavy-ion fragmentation is a complex process, which requires a great deal of understanding in fundamental physical theory of the scattering process. The rest of the chapter will now focus on the two studies, which form the basis of the current research effort. These are the original the works by Cucinotta et al [26] and Braley et al. [11]. In the following sections, brief derivations of the knockout-ablation cross sections are presented. More extensive details can be found in the references.

2.2. Knockout-Ablation Model

In this study, the knockout-ablation model (with extended approximations) is used for predicting secondary neutron and light ion production cross sections. The underlying physical concepts of the knockout-ablation process are briefly reviewed in the following subsections. The model is based upon an optical potential approximation to the quantum-mechanical Glauber multiple-scattering theory. The expression for secondary neutron production in both stages [10; 11; 110] is given in terms of the nucleon momentum distribution for each step:

$$\left(\frac{d\sigma}{d\mathbf{k}}\right)_{total} = \left(\frac{d\sigma}{d\mathbf{k}}\right)_{ko} + \left(\frac{d\sigma}{d\mathbf{k}}\right)_{abl} \tag{5}$$

where $\boldsymbol{k}$ is the wave number of the emitted neutrons and $\mathbf{p} = \hbar\boldsymbol{k}$ is neutron momentum. The subscripts *ko* and *abl* refer to knockout and ablation respectively. Note that the neutron cross sections produced from the ablation process can be separated into the elastic fragmentation and the spectator reaction [52]. The derivations of the nucleon momentum distribution for each reaction are discussed in the following subsections.

2.2.1. Knockout model

2.2.1.1. Glauber multiple-scattering theory

The fundamental theory in this work for the knockout (abrasion) cross section is based on the Glauber multiple-scattering formalism [55; 56] with the optical potential approximations. The main focus of this work uses the approximations developed by Cucinotta et al [26], Franco and Tekou [48], Hüfner et al. [67], Townsend [96], Wilson [110], Wilson and Townsend [114], and others. Abrasion is an inelastic scattering process [38; 67]. The nature of this step involves a number of nucleons from the projectile nucleus with relativistic momentum and energy colliding into a stationary target nucleus. In the collision a relatively small number of nucleons are removed and a considerable amount of energy deposited into the remaining prefragment [68]. This is similar to a Monte Carlo intra-nuclear cascade process [30]. The following derivation is a synopsis of the knockout stage presented in Cucinotta et al. [26]. Starting with the simplest type of the scattering problem, Glauber [56] presents the corresponding differential cross section as

$$\begin{aligned} d\sigma &= \frac{Flux\ through\ d\Omega}{Incident\ \ flux} = \left|f(\mathbf{q})\right|^2 d\Omega \\ \sigma_{scatt} &= \int \left|f(\mathbf{q})\right|^2 d\Omega \end{aligned} \tag{6}$$

where f($\mathbf{q}$) is the elastic scattering amplitude. For high energy particle collision, $d^2\mathbf{q}$ term is assumed to equal to $d^2\mathbf{k}$, and $\hbar\mathbf{q}$ is the momentum transfer. In the Glauber formalism with the Eikonal coupled-channels approximation, the heavy-ion scattering amplitude of a projectile P and a target T for a basic nucleon-nucleon (NN) collision is represented by

$$\overline{f}(\mathbf{q}) = \frac{i\,\mathbf{k}_N}{2\pi}\int d^2\mathbf{b}\ e^{i\mathbf{q}\cdot\mathbf{b}}\langle\Gamma(\mathbf{b})\rangle\,, \tag{7}$$

and

$$\Gamma(\mathbf{b}) = 1 - e^{i\overline{\chi}(\mathbf{b})} \tag{8}$$

where ħ**q** denotes as the momentum transfer, ħ$\mathbf{k}_N$ represents the incident momentum of a nucleon, **b** is the impact parameter vector perpendicular to the direction of the incident beam and Γ(**b**) is the profile function. In the case of the spin-independent nucleon scattering to a ground state, the nucleon-nucleon phase shift function $\overline{\chi}(\mathbf{b})$ can be expressed in matrix operators as [45]

$$e^{i\overline{\chi}(\mathbf{b})} = \left\langle \psi_P \psi_T \middle| \prod_{i,j}^{A_P A_T} \left[1 - \Gamma_{ij}\left(\mathbf{b} - \mathbf{s}_i - \mathbf{s}_j\right)\right] \middle| \psi_P \psi_T \right\rangle \tag{9}$$

where i and j denote as the projectile and target constituents, ψ_P and ψ_T are the nuclear wave functions of the projectile and target and $\Gamma_{i,j}\ (\boldsymbol{b} - \boldsymbol{s_i} - \boldsymbol{s}_j)$ represents the nucleon-nucleon profile function for the collision of the projectile nucleon i located at $\mathbf{s}_i$ and the target nucleon j located at $\mathbf{s}_j$. The $\mathbf{s}_i$ and $\mathbf{s}_j$ refer to the projectile and target center of mass where the projectile moves in the $\boldsymbol{z}$ direction. Note that the phase shift function $\overline{\chi}(\mathbf{b})$ can be expressed in terms of the Fourier transform inverse function as [21]

$$\overline{\chi}(\mathbf{b}) = \frac{1}{2\pi \mathbf{k}_{NN}} \sum_{i,j} \int d^2\mathbf{q}\ e^{i\mathbf{q}\cdot\mathbf{b}} e^{i\mathbf{q}\cdot\mathbf{s}_i} e^{i\mathbf{q}\cdot\mathbf{s}_j} f_{NN}(\mathbf{q}) \tag{10}$$

where f_{NN} is the nucleon-nucleon (*NN*) scattering amplitude and $\boldsymbol{k}_{NN}$ is the *NN* relative wave number. (Appendix A contains more detail of the derivation of the optical limit functions.)

2.2.1.2. Differential cross section

The development in this section follows closely that presented in Cucinotta et al [23; 26] and references therein. Eq. (6) is expanded using the relationship of the scattering amplitude in eq. (7) and the kinematical phase space of nucleon in each state. The differential cross section for the scattered nucleon is then given as

$$d\sigma = \frac{(2\pi)^4}{\beta} \sum_X d\mathbf{p}_X\, d\mathbf{p}_{F^*} \sum_{n=1} \prod_{j=1}^{n} d\mathbf{p}_j\ \delta(E_i - E_f)\ \delta(\mathbf{p}_i - \mathbf{p}_f)\ \left|T_{fi}\right|^2 \tag{11}$$

where $\mathbf{p}_X$ denotes as the single momentum vector for all states, β is the relative projectile target velocity, F^* is the excited prefragment, n is the number of nucleons abraded from the projectile in the overlap region with the target, and i and f denote the initial and final states, respectively. The term T_{fi} denotes the nuclear matrix element between initial and final states. The parameter $d\mathbf{p}_{F^*}$ is defined as

$$d\mathbf{p}_{F^*} = d\mathbf{p}_F \prod_{r=0} d\mathbf{p}_r \tag{12}$$

where r denotes the ions emitted in the ablation process. When energy-momentum conservation in the projectile rest frame is treated, the phase space momentum can be transformed into the momentum transfer of each state. The cross section then becomes

$$d\sigma = (2\pi)^4 \sum_X d\mathbf{q}_T \, S \prod_{r=0} d\mathbf{p}_r \sum_{n=1} \prod_{j=1}^{n} d\mathbf{q}_j \left|T_{fi}\right|^2 \tag{13}$$

where $\mathbf{q}_T$ is the transverse momentum transfer, $\mathbf{q}_L$ is the longitudinal momentum transfer, $\mathbf{q}_j$ is the momentum transfer for each state and the phase space factor S is defined as

$$S = \frac{1}{\beta}\left(\frac{-\partial E_f}{\partial q_L}\right). \tag{14}$$

The momentum distribution for the projectile-target scattering is derived by differentiating eq. (11) as

$$\frac{d\sigma}{dp} = (2\pi)^4 \sum_X \int d\mathbf{q}_T \sum_{n=1} \int \prod_{j=2}^{n} d\mathbf{p}_j \prod_{r=0} d\mathbf{p}_r \, S \left|T_{fi}\right|^2 . \tag{15}$$

The expression above can be replaced by $S = \int dq_L \, \delta(E_i - E_f) \rightarrow \int dE_{F^*} \, \delta(E_i - E_f)$, expanding the nuclear wave function into the matrix representation at the ground state, and then rearranging into

$$\begin{aligned} \frac{d\sigma}{d\mathbf{k}} = \left(\frac{1}{2\pi}\right)^2 \sum_X \int dE_{F^*} \, d^2q \, d^2b \, d^2b' e^{i\mathbf{q}\cdot(\mathbf{b}-\mathbf{b}')} \, \delta(E_i - E_f) \, \times \\ \int \prod_{j=2}^{n} \left[\frac{dk_j}{(2\pi)^3}\right] \langle TP \,|\Gamma'(\mathbf{b}')|\, XF^*\mathbf{k}_j\rangle \, \langle \mathbf{k}_j F^* X \,|\Gamma(\mathbf{b})|\, PT\rangle \end{aligned} \tag{16}$$

where E_{F^*} is the prefragment excitation energy, $\boldsymbol{k}_j$ is the wave number vector of abraded nucleon, P denote as the projectile, and T and X represent the initial and final target states, respectively. At high energy and summing over $\left|X\right\rangle$, the momentum distribution is found as

$$\frac{d\sigma}{d\mathbf{k}} = \left(\frac{1}{2\pi}\right)^2 \int dE_{F^*}\, d^2q\, d^2b\; d^2b'\, e^{i\mathbf{q}\cdot(\mathbf{b}-\mathbf{b}')}\, \sigma_n(\mathbf{b},\mathbf{b}',\mathbf{k},\mathbf{q},E_{F^*})\,. \tag{17}$$

The parameter W_n is described by the plane wave of the momentum $\boldsymbol{k}_j$ and energy as

$$\sigma_n(\mathbf{b},\mathbf{b}',\mathbf{k},\mathbf{q},E_{F^*}) = \langle T| \left\{ \begin{array}{l} \int \prod_{j=2}^{n} \left[\frac{d\mathbf{k}_j}{(2\pi)^3}\right] \delta(E_i - E_f) \\ \langle P|\Gamma'(\mathbf{b}')|F^*\mathbf{k}_j\rangle\langle \mathbf{k}_j F^*|\Gamma(\mathbf{b})|P\rangle \end{array} \right\} |T\rangle\,. \tag{18}$$

Note that the delta function term describes the conservation in energy from the initial to the final state during the momentum transfer and the $E_i - E_f$ term is defined as

$$E_i - E_f = \varepsilon_B - \sum_{j=2} \frac{\mathbf{k}_j^2}{2m_N} \tag{19}$$

where ε_B is the energy lost by the projectile (which include the energy transferred from the initial to final states), and the second term is the total energy loss in the collision. Introducing the Fourier transform pair of $R_n(E)$:

$$R_n(t) = \int d\omega\, e^{-i\omega t} R_n(\omega) \qquad and \qquad R_n(\omega) = \int \frac{dt}{2\pi}\, e^{i\omega t}\, R_n(t)\,, \tag{20}$$

Eq. (18) becomes

$$\sigma_n(t) = \langle T \left| \left\{ \begin{array}{l} \int \prod_{j=2}^{n} \left[\frac{d\mathbf{k}_j}{(2\pi)^3}\right] e^{-i\varepsilon_B t} e^{i\sum_{j=2} \mathbf{k}_j^2 t/2m_n} \\ \langle P|\,\Gamma'(\mathbf{b}')\,|F^*\mathbf{k}_j\rangle\langle \mathbf{k}_j F^*|\,\Gamma(\mathbf{b})\,|P\rangle \end{array} \right\} \right| T\rangle \tag{21}$$

The assumption of no observation of the final state of the target in the abrasion model is applied. There are n nucleons knocked out from A_p projectile nucleons, and therefore $A_{F^*} = A_p - n$. The relationship of the knockout participants and the core spectator is used to separate the wave functions into more simple forms as

$$\sigma_n(t) = \langle T| \left\{ \begin{array}{l} \binom{A_P}{n} \langle F|\, \prod_j Q_j^+(\mathbf{b}' - \mathbf{s}_j')\, |F^*\rangle\, \langle F^*|\, \prod_j Q_j(\mathbf{b} - \mathbf{s}_j)\, |F\rangle \\ \qquad \times \int d\mathbf{r}_1 d\mathbf{r}_1'\, e^{i\mathbf{k}_1\cdot\mathbf{x}_1} Q_1^+(\mathbf{b}' - \mathbf{s}_1') Q_1(\mathbf{b} - \mathbf{s}_1) \prod_{j=2}^{n} [\int \frac{dk_j}{(2\pi)^3} d\mathbf{r}_j d\mathbf{r}_j' \\ \qquad \times e^{i\mathbf{k}_j\cdot\mathbf{x}_j} e^{-i\varepsilon_B t}\, e^{-k_j^2 t/2m_N} Q_j^+(\mathbf{b}' - \mathbf{s}_j') Q_j(\mathbf{b} - \mathbf{s}_j)] \\ \qquad \times \phi_n^+(\mathbf{r}_1', \cdots, \mathbf{r}_n')\; \phi_n(\mathbf{r}_1, \cdots, \mathbf{r}_n) \end{array} \right\} |T\rangle \tag{22}$$

where $\boldsymbol{x}_j = \mathbf{r}_j - \mathbf{r}'_j$ (the internal coordinate components) and $Q = \prod_{\zeta=1}^{A_T}(1-\Gamma_{\zeta,j})$. Rearranging eq. (22) into the probability distribution function for the abrasion process using coherent approximation for target wave function in intermediate states and the independent particle model for the fragment wave function, the cross section for the abraded nucleons can be expressed in simple form as

$$\sigma_n(t) = \binom{A_P}{n} P^{A_P-n}(\mathbf{b},\mathbf{b}')\,\Lambda_{n-1}(\mathbf{b},\mathbf{b}',t)\frac{dN_1}{d\,\mathbf{k}} \tag{23}$$

where the probability function for the projectile spectator is given as

$$P^{A_P-n}(\mathbf{b},\mathbf{b}') = \langle\, T\,F \mid \prod_j Q_j^+(\mathbf{b}'-s'_j) \Big| F^*\rangle\,\langle\, F^* \Big| \prod_j Q_j(\mathbf{b}-s_j) \mid F\,T\,\rangle\,, \tag{24}$$

and the target response function is defined

$$\Lambda_{n-1}(\mathbf{b},\mathbf{b}',t) = \langle T \Big| \left\{ \int\prod_{j=2}^{n} \begin{bmatrix} d\mathbf{r}_j d\mathbf{r}'_j \left(\dfrac{m_N}{2\pi i t}\right)^{\frac{3}{2}} e^{\frac{-m_n x_j^2}{2it}} \rho(\mathbf{r}_j,\mathbf{r}'_j) \\ \times Q_j^+(\mathbf{b}'-\mathbf{s}'_j)\,Q_j(\mathbf{b}-\mathbf{s}_j) \end{bmatrix} \right\} \Big| T\rangle\,. \tag{25}$$

The response function in eq. (25) is transformed into energy space as

$$\Lambda_{n-1}(\mathbf{b},\mathbf{b}',T_{F^*},k) = \langle T \Big| \left\{ \int\prod_{j=2}^{n} \begin{bmatrix} d\mathbf{r}_j d\mathbf{r}'_j \rho(\mathbf{r}_j,\mathbf{r}'_j)\,Q_j^+(\mathbf{b}'-\mathbf{s}'_j)\,Q_j(\mathbf{b}-\mathbf{s}_j) \\ \times \dfrac{m_N}{2}\left(\dfrac{1}{2\pi}\right)^{\frac{3(n-1)}{2}} \dfrac{\xi_{n-1}^{[3(n-1)/2]-1}}{\bar{x}_{n-1}^{[3(n-1)/2]-1}} \\ \times J^1_{[3(n-1)/2]}(\xi_{n-1}x_{n-1}) \end{bmatrix} \right\} \Big| T\rangle \tag{26}$$

where J^1_m is the cylindrical Bessel function of the first kind of order m and T_{F^*} is the recoil energy of prefregment. The parameter $\rho(\boldsymbol{r}, \boldsymbol{r}')$ is the projectile one-body density matrix, given as $\rho(\boldsymbol{r}, \boldsymbol{r}') = \phi^+(\boldsymbol{r}')\,\phi(\boldsymbol{r})$ given that ϕ is the ground-state single-particle wave function. Assuming the projectile remains in the ground state throughout the collision, the energy transfer term becomes

$$\xi_{n-1} = \sqrt{2\,m_n(\varepsilon_B - \mathbf{k}^2/2m_N)}\,, \tag{27}$$

and the coordinate $\bar{x}_{n-1}$ becomes

$$\bar{x}_{n-1} = \sqrt{\sum_{j=2}^{n} x_j^2} \ . \tag{28}$$

Assuming forward-peaked density matrices and a small argument expansion of the Bessel functions [21; 22; 23; 26], the response function for a target becomes

$$\begin{aligned}\Lambda_{n-1}\left(\mathbf{b},\mathbf{b}',T_{F^*},\mathbf{k}\right) \approx C_{n-1}\left[T_{F^*} + \frac{\mathbf{k}^2}{2m_n} - S_n - (E_T - E_X)\right]^{n-1} \\ \times \Lambda_1^{n-1}\left(\mathbf{b},\mathbf{b}',\frac{\xi_{n-1}}{\sqrt{n-1}}\right) + O(\xi^4 x^4)\end{aligned} \tag{29}$$

where some sample of quantities C_{n-1} are given as $C_1 = 1$, $C_2 = \pi/4$, $C_3 = \pi/105$ and $C_4 = \pi^2/240$.

The last term in eq. (23) is defined as

$$\frac{dN_1}{d\mathbf{k}} = \frac{1}{(2\pi)^3}\int d\mathbf{r}\, d\mathbf{r}'\, e^{i\mathbf{k}\cdot\mathbf{x}}\ \rho(\mathbf{r},\mathbf{r}') Q_j^+(\mathbf{b}'-\mathbf{s}')\ Q_j(\mathbf{b}-\mathbf{s}) \ . \tag{30}$$

2.2.1.3. Knockout total cross section

Substituting all the definitions for eq. (23) into eq. (17), the nucleon momentum distribution from knockout process is expressed as

$$\begin{aligned}\left(\frac{d\sigma}{d\mathbf{k}}\right)_{ko} = \sum_n \binom{A_P}{n} \frac{1}{(2\pi)^2}\int d^2q\, d^2\mathbf{b}\, d^2\mathbf{b}' e^{i\mathbf{q}\cdot(\mathbf{b}-\mathbf{b}')}\ P^{A_p-n}(\mathbf{b},\mathbf{b}') \\ \frac{dN_1}{d\mathbf{k}}\int dT_{F^*}\Lambda_{n-1}(\mathbf{b},\mathbf{b}',T_{F^*},\mathbf{k})\end{aligned} \ . \tag{31}$$

At very high energy, the approximation of eq. (31) becomes

$$\left(\frac{d\sigma}{d\mathbf{k}}\right)_{ko} = \sum_n \binom{A_P}{n} \frac{1}{(2\pi)^2}\int d^2b\, P^{A_p-n}(\mathbf{b})\ \frac{dN_1}{d\mathbf{k}}\int dT_{F^*}\Lambda_{n-1}(\mathbf{b},T_{F^*},\mathbf{k}) \tag{32}$$

where the first collision term is modified to include the effect of final-state interactions from the abraded nucleons using the Eikonal approximation described in Cucinotta [23] as

$$\frac{dN_1}{d\mathbf{k}} = \frac{1}{(2\pi)^3}\int d\mathbf{r}\, d\mathbf{r}'\, e^{i\mathbf{k}\cdot\mathbf{x}} e^{-2\,\mathrm{Im}\,\chi^- y} \rho(\mathbf{r},\mathbf{r}')\, Q_j^+(\mathbf{b}'-\mathbf{s}')\, Q_j(\mathbf{b}-\mathbf{s}) \tag{33}$$

where χ^- is the outgoing Eikonal phase [25]. Considering the concept of an inclusive nucleon production originating from the projectile, the inclusive momentum distribution is given from eq. (32) as

$$\left(\frac{d\sigma}{d\mathbf{k}}\right)_{ko} = \sum_n \binom{A_P}{n} \int d^2\mathbf{b}\, P^{A_p - n}(\mathbf{b})\, \frac{dN_n}{d\mathbf{k}} \tag{34}$$

where
$$\frac{dN_n}{d\mathbf{k}} = \frac{dN_1}{d\mathbf{k}}\left[1 - P(\mathbf{b})\right]^{n-1} \tag{35}$$

and
$$\int \frac{dN_1}{d\mathbf{k}}\, d\mathbf{k} = 1 - P(\mathbf{b})\,. \tag{36}$$

The total abrasion cross section for abrading *n* nucleons is then expressed as

$$\sigma_{ko} = \binom{A_P}{n} \int d^2\mathbf{b}\, P^{A_p - n}(\mathbf{b})\, \left[1 - P(\mathbf{b})\right]^n . \tag{37}$$

2.2.2. Ablation model

In the ablation stage, the prefragment nuclei give up their excess energies by evaporating fragment nucleons, light-ion clusters and gamma rays while decaying into the ground state [68]. Due to the complexity of the process related to prefragment thermalization, temperature dependence of fragments, and the underlying physics of the evaporation model, the expressions for the ablation step are more difficult to develop. In this work, the derivation of the ablation cross section follows closely the approach described in Cucinotta et al. [26], which in sequence follows the fundamental approaches presented in several previous studies [25; 37; 70; 77; 78; 82; 106]. One of previously mentioned studies [100] indicated that the rate that the prefragment decays by emission of nuclear particles depends on the magnitude (or strength) of the excitation energies. Considering the excitation spectra as using average energies, the neutron spectrum from the ablation process is calculated using a Weisskopf-Ewing statistical decay model. The secondary neutron momentum distribution in the projectile rest frame is written as

$$\left(\frac{d\sigma}{d\mathbf{k}}\right)_{abl} = \sum_j \sigma_{abr}\left(A_j, Z_j, E_j^*\right) P_n\left(j, \mathbf{k}\right) \tag{38}$$

where the total abrasion cross section is derived from eq. (37) and P_n $(j,\boldsymbol{k})$ is defined as the probability that a prefragment labeled j with mass number A_j, charge number Z_j, and the excitation energy E_j^*, emits a nucleon with momentum $\mathbf{k}$. To simplify the calculation of the probability term, the prefragment mass is assumed to be substantially large. The assumption of isotropic emission spectrum is also applicable for the statistical model [70; 106]. The probability function then becomes [70]

$$P_n(j, E_n) = \frac{2\mu_n g_n E_n \sigma_{CN} w_0(E_j^* - E_n)}{\sum_l F_l} \tag{39}$$

where μ_n is the neutron reduced mass, g_n is the statistical weight, σ_{CN} is the formation cross section by the inverse process, and w_0 is the level density of the residual nucleus. The denominator in eq. (39) is defined as

$$F_l = \int_0^{E_l^* - S_j} P_l(j, E)\, dE\,. \tag{40}$$

As mentioned previously all of the calculations are done in the projectile rest frame. To transform the neutron production into the lab frame, the neutron cross sections for ablation in eq. (38) are multiplied by the neutron energies to form Lorentz invariant cross sections which have the same values in all reference frames.

2.3. Coalescence model

The development of the coalescence formalism described in the following section is a synopsis of the theory presented by Awes et al. [1]. The concept of the composite particle production as part of high-energy heavy-charged particle collisions has been reported in the context of empirical and theoretical studies [12; 13; 60; 62; 72; 91]. The basic physical assumption of the coalescence model is that during high-energy heavy-charged particle reactions the secondary light ions (also known as composite particles) are produced by the coalescence of particles which happen to share the same volume and momentum space. Coalescence of nucleons was first introduced by Butler and Pearson [13] as the coalescence of cascade nucleons, and later was modified by Schwarzschild and Zupančič [91] to include the production of light ions such as the deuteron from the interactions among the secondary cascade nucleons and with the nuclear field, and as a result, the excess momentum and energy are transferred. Based on the theoretical formalism presented by both studies, Awes et al. [1] introduced the coalescence model using a Poisson distribution to calculate the composition of the secondary light ions. The probability P for finding one primary nucleon in the coalescence volume centered at a momentum per nucleon $\mathbf{p}$ is given by the product of this volume with the single nucleon momentum density

$$P = \frac{4\pi}{3} p_0^3 \frac{\gamma}{\overline{m}} \frac{d^3 N(\mathbf{p})}{d p^3} \tag{41}$$

where $d^3 N(\mathbf{p}) / d p^3$ denotes the differential nucleon multiplicity, p_0 is the critical radius for coalescence in the momentum space, $\overline{m}$ is the average nucleon multiplicity, and γ = 1+T/m (c ≡ 1). Assuming an independent probability for the observation of neutrons and protons, the average probability for finding N neutrons and Z protons in the coalescence volume is

$$\langle P(N,Z) \rangle = \frac{(\overline{m}_Z P_Z)^Z}{Z!} \frac{(\overline{m}_N P_N)^N}{N!} . \tag{42}$$

The parameter $P(N,Z)$ in eq. (42) represents the probability of forming composite particles in the coalescence volume. The neutron distribution therefore is calculated by multiplying the weighted ratio N/Z of the composite particles to the proton distributions of that system as

$$\frac{d^3 N(0,1)}{d p^3} = \frac{N_P + N_T}{Z_P + Z_T} \frac{d^3 N(1,0)}{d p^3} \tag{43}$$

where N_p and N_t are the projectile and target neutron numbers, and Z_p and Z_t are the projectile and target charge numbers. Substituting eqs. (41) and (43) into eq. (42) and dividing by the coalescence volume, the differential composite multiplicity at relativistic energies is given as

$$\frac{d^3N(Z,n)}{dp^3} = \frac{1}{N!Z!}\left(\frac{N_P + N_T}{Z_P + Z_T}\right)^N \left(\frac{4\pi\gamma}{3}p_0^3\right)^{A-1}\left[\frac{d^3N(1,0)}{dp^3}\right]^A \tag{44}$$

where Z, n, and A are the composite particle charge, neutron number and mass, respectively. Note that $d^3N(\mathbf{p})/dp^3$, the differential nucleon multiplicity per event, is related to the nucleon momentum distribution by

$$\frac{d^3N}{dp^3} = \frac{1}{\sigma_0}\frac{d^3\sigma}{dp^3} = \frac{1}{\sigma_0}\frac{d^3\sigma}{p^2dp\,d\Omega} \tag{45}$$

where σ_0 is the projectile-target total reaction cross section. It is also important to note that the evaluation of the neutron differential cross section and its momentum distribution occurs in the rest frame of the projectile. However, all differential cross sections are required to be evaluated in the laboratory rest frame or the center of mass frame. The Lorentz invariant differential cross section is related to the double differential cross section as

$$E_n\frac{d^3\sigma}{dp^3} = \frac{1}{p_n}\frac{d^2\sigma}{dE_n\,d\Omega_n} \tag{46}$$

where E_n, p_n, Ω_n are kinetic energy, momentum, and direction of nucleon n in the laboratory rest frame. To transform the composite spectrum into the lab rest frame using the Lorentz invariant technique, eq. (44) is substituted into eq. (45), and then converted to the Lorentz invariant cross section of the composite system using eq. (46). The double differential momentum distribution is expressed as

$$\frac{d^2\sigma(Z,n)}{dE_n\,d\Omega} = R(Z,n)\,\frac{d^2\sigma(n)}{dE_n\,d\Omega} \tag{47}$$

where

$$R(Z,n) = \frac{A^2}{N!Z!}\left(\frac{n_P + n_T}{Z_P + Z_T}\right)^N \left(\frac{4\pi\,p_0^3}{3\sigma_0 p_n\,m}\right)^{A-1}. \tag{48}$$

Note that the critical radius p_0 previously mentioned is treated as a free parameter derived from experimental observation. A wide range values for p_0 have been proposed. In this work, results presented are based on calculations with values of p_0 described in Awes et al. [1] and Nagamiya et al. [79].

3. PREVIOUS UBERNSPEC WORK

3.1. Work of Cucinotta and collaborators

The following is adapted from Cucinotta et al. [26], which presented an extended version of the original abrasion-ablation model by Hüfner et al. [67] to calculate momentum distributions for nucleon production in heavy ion collisions. The model also included a calculation of the energy spectrum of the knockouts (the abrasion process) in the overlap region of the collision using the optical potential approximation applied in Glauber multiple-scattering theory. The calculation of the neutron production from the ablation stage is based upon the estimation of excitation energies from the abrasion stage using the classical evaporation model. To some extent the physics of this model is similar to that in intranuclear cascade codes that use Monte Carlo methods [30; 57; 67]. In the ablation process, furthermore, the concept of frictional spectator interaction (FSI) energy is introduced and the contribution from FSI energies is included in final calculations. The FSI concept is based on the assumption that some abraded nucleons from the projectile are scattered into rather than away from the prefragment and cause additional excitation energy deposition. The abrasion-ablation formalism in this work is also extended to the treatment of the single-particle nuclear wave functions for all stages. Although several changes were made, this formalism is much simpler as it contains a few numerical integrations and can be used to test nuclear structure inputs such as the one-body density matrix. The model calculations include up to third-order terms in the evaporation cascade effects for projectile knockouts interacting with the projectile prefragment. The production of nucleons from the decay of nucleon isobars is not included in the calculations.

The sample calculations from Cucinotta et al. [26] showed in Figures 3.1 - 3.2 present neutron production from 390 MeV/nucleon and 800 MeV/nucleon ^{20}Ne beams colliding with targets of NaF and Pb compared with the experimental data from Madey and collaborators [73; 74]. (The NaF target is represented by ^{20}Ne.) The calculations

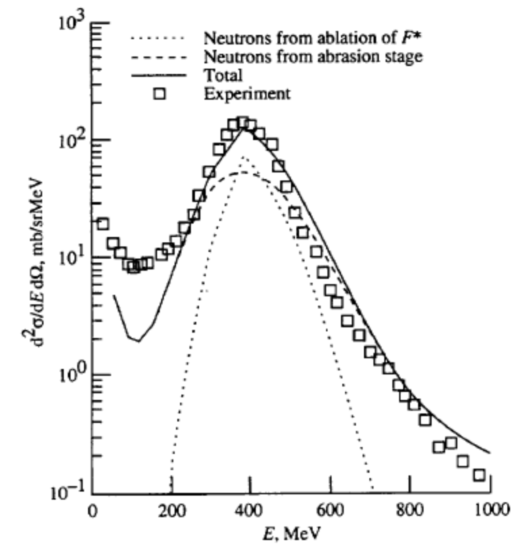

Figure 3.1: Comparison between calculations and experimental data for the energy spectrum of secondary neutrons for 390 MeV/nucleon Ne colliding with NaF targets at 0° in the laboratory frame. This work was originally presented in Cucinotta et al. [26].

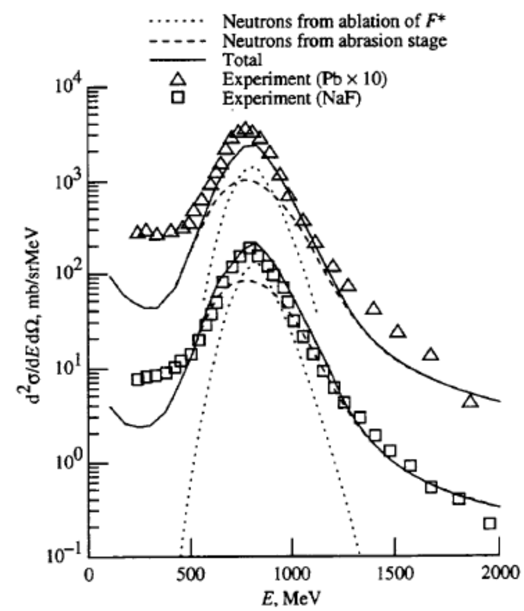

Figure 3.2: Comparison between calculations and experimental data for the energy spectrum of secondary neutrons for 800 MeV/nucleon Ne beams colliding with NaF and Pb targets at 0° in the laboratory frame. This work was originally presented in Cucinotta et al. [26].

demonstrate that there is significant neutron production in both abrasion and ablation stages and that there is good agreement with the experimental data for forward angle neutron production. Note that the underestimates of neutron production below 200 MeV in Figure 3.1 and 500 MeV in Figure 3.2 are primarily due to the neglect of the isobar channel.

3.2. Work of Braley and collaborators

Braley et al. [11] improved the knockout-ablation model by incorporating coalescence effects into the formalism and included the contribution of ablated nucleons from the target prefragments. The basic assumption of coalescence is that during the knockout and ablation stages there are some nucleons that share the same physical volume and momentum space and they interact with each other to form heavier and more complex particles such as deuterons, tritons, helions, and alphas. The details of the coalescence formalism in UBERNSPEC are presented in the next chapter. The improved model was used to calculate neutron production from several energies and reactions and compared with the published measurements [73; 89]. The comparisons of neutron energy spectrum of 135 MeV/nucleon ^{12}C and ^{12}C reactions at 0° and 50° in the laboratory are shown Figures 3.3 and 3.4. Figure 3.5 also shows a comparison of the neutron spectrum for Ne and NaF reaction at 390 MeV/nucleon at 0° in the laboratory. The open squares represent the experimental data reported in [73; 89]; the filled squares represent the predictions without coalescence; and the filled diamonds represent the predictions with coalescence effects. Incorporating the coalescence effects into the abrasion-ablation model shows an improvement of the neutron predictions from the abrasion-ablation model above the beam energy per nucleons. There is some disagreement, however, between the predictions from the improved model and the measurements at below beam energy. This is probably due to the need to account for neutrons produced by isobar formation and decay in the model. In the overall aspect, the model demonstrates fair predictions of secondary neutrons at the velocities greater than the incident beam velocity, except for the 50° predictions in Figure 3.4.

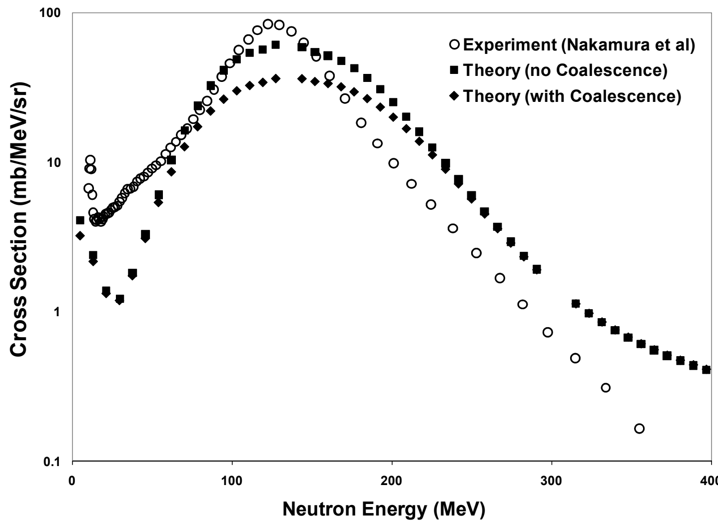

Figure 3.3: Comparison of predicted double differential neutron cross sections and energy spectrum with measurement data for 135 MeV/nucleon $^{12}C + ^{12}C$ reaction at 0° in the laboratory. The open circles represent experimental data; the filled squares are calculations without the coalescence effect; and the filled diamonds are calculations with the coalescence effects. This work was initially presented in Braley et al. [11].

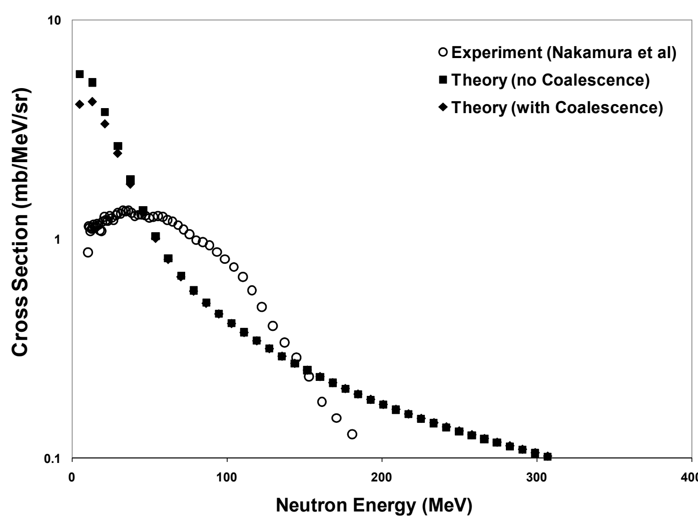

Figure 3.4: Comparison of predicted double differential neutron cross sections and energy spectrum with measurement data for 135 MeV/nucleon $^{12}C + ^{12}C$ reaction at 50° in the laboratory. The open circles represent experimental data; the filled squares are calculations without the coalescence effect; and the filled diamonds are calculations with the coalescence effects. This work was initially presented in Braley et al. [11].

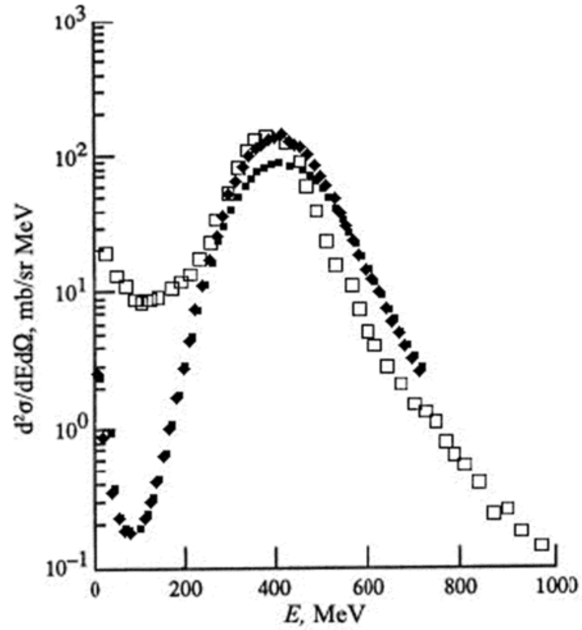

Figure 3.5: Comparison of predicted double differential neutron cross sections and energy spectrum with measurement data for 390 MeV/nucleon Ne + NaF reaction at 0° in the laboratory. The open circles represent experimental data; the filled squares are calculations without the coalescence effect; and the filled diamonds are calculations with the coalescence effects. This work was initially presented in Braley et al. [11].

4. CURRENT UBERNSPEC CODE STATUS

4.1. UBERNSPEC code

4.1.1 General description

Based on the knockout-ablation-coalescence formalism described in the previous chapter the analytical computer code UBERNSPEC was developed. It is used for calculating the Lorentz-invariant and double differential cross sections (energy and angle) of the secondary neutrons and the composite particles produced in nucleon-nucleus and nucleus-nucleus collisions. The model has been programmed in the FORTRAN computer language. It was initially developed on a VAX-11/785 minicomputer using the VAX/VMS operating system at NASA Langley Research Center. The current version operates on a standard personal computer using the Windows® operating system and is executed using the Compaq Visual FORTRAN Compiler program. The present version of the UBERNSPEC code involves both FORTRAN 77 and 90 languages. The code consists of a main program, 40 subroutines, and 13 function modules, which are combined into 3,380 lines of code. Figures 4.1.a and 4.1.b display the calling structure in detail for the main program and all the subprograms (subroutines and functions).

4.2. General comparisons with NASA HZE fragmentation codes

Heavy-ion fragmentation collisions at high energy have been studied for the past 60 years, and several approaches to the solution of these HZE interaction processes have been developed. The development of accurate high-energy heavy-ion cross section databases and libraries are necessary to obtain reliable space radiation shielding and health risk assessments when using high-energy space radiation transport codes. There are several analytical nuclear models and computational nuclear cross section codes

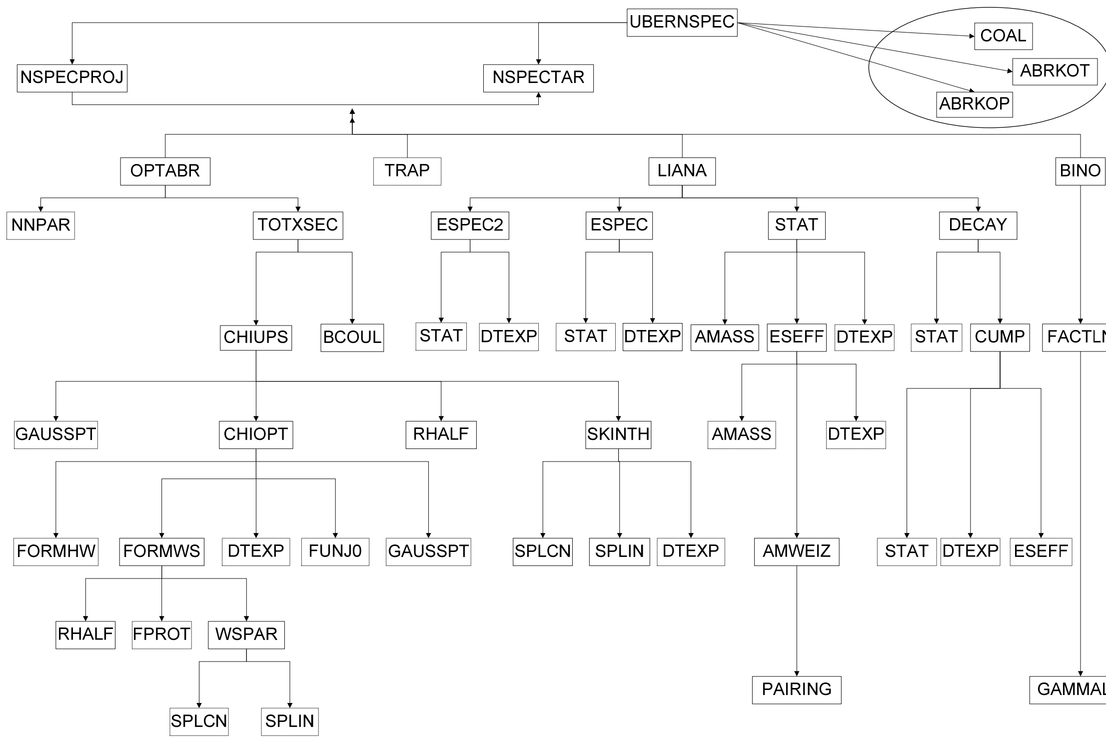

Figure 4.1.a: Calling structure of the UBERNSPEC code for the main program, subroutines and function modules. Note that the expansions of the ABRKOP, ABRKOT and COAL subroutines listed in the oval in the upper right corner are shown in detail in the next schematic (Figure 4.1.b)

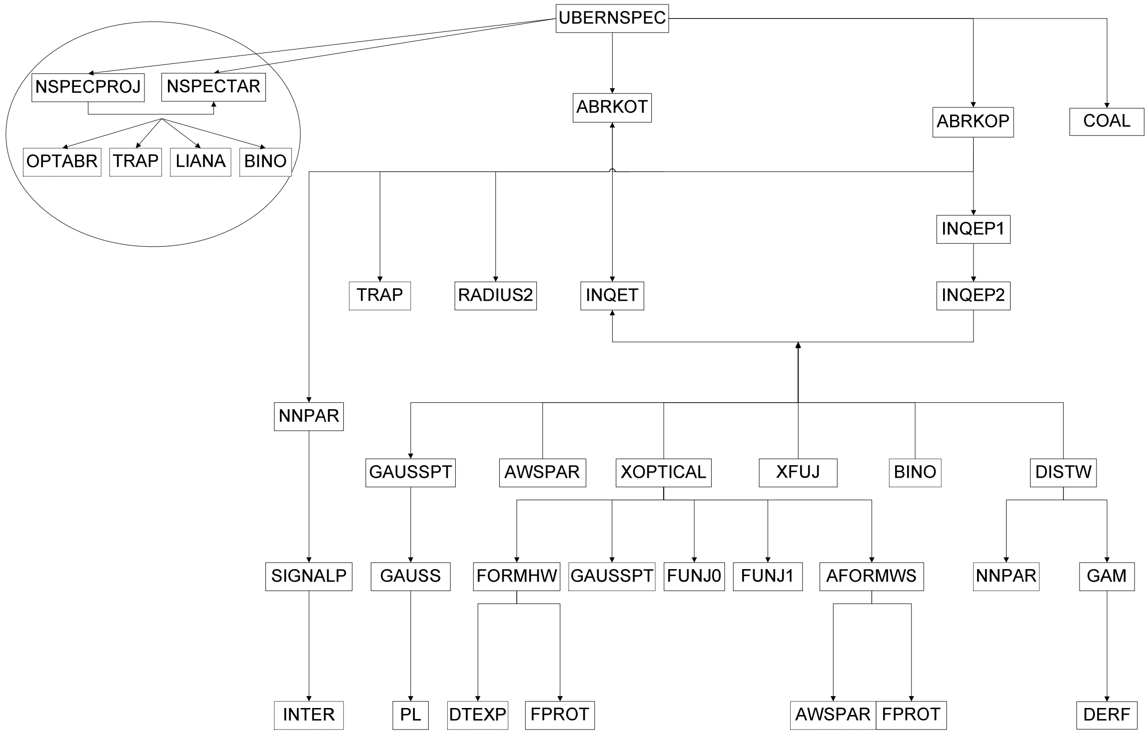

Figure 4.1.b: Calling structure of the UBERNSPEC code for the main program, subroutines and function modules. In this diagram, the ABRKO, COAL and NSPECTAR subroutines and their call function modules are clearly shown in detail. The call structure of the NSPECPROJ and NSPECTAR subroutines in the upper left corner oval is displayed in detail in Figure 4.1.a.

related to high-energy heavy-ion fragmentation interactions developed by NASA researchers. The first NASA library of heavy-ion cross sections was developed by Wilson and Costner [111] [120]. In this section, discussions and comparisons will be limited only to the NUCFRG2 [117; 120] and QMSFRG [27; 29] nuclear fragmentation computational codes, which are currently used in the NASA space radiation transport codes.

4.2.1. The NUCFRG2 model

NUCFRG2 is a semiempirical nuclear fragmentation computer program that predicts nuclear fragmentation cross sections from the collisions of heavy nuclear fragments (A > 4). The NUCFRG2 model [117; 120] was based on the classical geometric overlapping approach presented in the abrasion-ablation model by Bowman et al. [10]; the method was extended by adding the following corrections: (1) a semiempirical higher-order correction for the surface deformation energy of the abrasion products; (2) electromagnetic dissociation effects which are important for interactions of heavy nuclei at high-energy; (3) the nuclear transmission factor accounting for the mean free path in nuclear matter; (4) the distributions of energy transfer across an interaction boundary; and lastly (5) the Rudstam formalism [88] for approximating the final charge distribution of the fragmentation products. The current version by Wilson et al. [120] included additional improvements, such as a maximum transmission factor in the overlap region, pre-equilibrium emission of spectator nucleons in abraded fragments, a unitarity correction for a target larger than mass number 63, and finally the semiempirical correction for distortion in the surface energy for light projectiles. Townsend and Cucinotta [102] reported that the cross section predictions using NUCFRG2 yielded general agreement within 25% with published experimental isotope production cross sections. Elemental production cross-section comparisons between predictions and measurements had even better agreement. Miller [76] also suggested that although, the NUCFRG2 accurately accounts for all the yields from both light ion and heavy ion fragments produced by nucleus-nucleus collisions of nucleon mass number A > 4, it poorly predicted the nuclear yields from light ion fragmentation interactions. There is a need to incorporate a correction for prediction production cross section from the fragmentation of nuclei mass number 2, 3 and 4 into the current model. Since the NUCFRG2 code is based on a semiempirical formulation, the resultant predictions are in the form of total yields and production cross sections. The model does not include the calculations of spectral or angular distributions for the secondary fragmentation, and as a result it is limited to primary heavy-ion production. For future space applications using three dimensional transport models, the contributions of secondary high-energy heavy-ion particles and light ions are essential and a means of incorporating differential energy and angular production cross sections into the model is needed.

4.2.2. The QMSFRG model

The QMSFRG code was first presented in Cucinotta et al. [27] as a heavy-ion fragmentation model for galactic cosmic rays studies. Unlike the NUCFRG2 code, which extends some additional terms and corrections in the geometric overlap approach describing the abrasion-ablation model [10], the QMSFRG model is based on the quantum-mechanical multiple-scattering theory by Glauber [55]. The earlier works of Cucinotta [24] and Cucinotta and Dubey [25], which relate to nuclear cluster production, specifically the α-cluster knockout and proton production at large forward momentum, help construct the analytical ground work for the QMSFRG code. The formulation for treating the interactions of prefragment nuclei with the abraded target was derived by using energy conservation in the abrasion process, a coherent approximation on the target final states, and neglect of longitudinal momentum transfers [27]. In the more recent work by Cucinotta and collaborators [29], modifications of the QMSFRG code were presented by incorporating the production of light ions through the abrasion, ablation, coalescence and nuclear cluster knockout processes. To some extent, this version of the QMSFRG appears to be similar to the current UBERNSPEC code. The resultant fragmentation cross sections from the QMSFRG are expressed in form of total, angular and energy dependent distributions.

4.3. Modification of the UBERNSPEC code

As described in previous sections, Cucinotta et al. [26] derived a modified abrasion-ablation-FSI formalism with inclusive momentum distributions of the secondary neutrons. Braley et al. [11] extended Cucinotta and collaborators' approach by partially incorporating coalescence effects into the model. The FORTRAN program that implemented this numerical model became known as the UBERNSPEC code. It was able to calculate secondary neutron production for nucleon-nucleus and nucleus-nucleus scattering interactions, including coalescence effects on the neutron distributions. In the present work, significant modifications to improve the UBERNSPEC code include for the first time: (1) the extension of the coalescence formulation to incorporate the effects of α particle coalescence, (2) the extension of the coalescence model to actually predict energy and angular distributions of light ions (*deuterons, tritons, helions, and alphas*), and (3) extending the capabilities of the code to predict secondary particle production cross section for collisions involving nuclei that have mass numbers greater than 68 were made. To accomplish these tasks required

a. Reformulating the coalescence model in the code by developing the expressions based on Lorentz invariant cross sections rather than double differential cross sections.
b. Extending the code to include the contribution of α production in the coalesced volume.
c. Finding and correcting coding errors in the ablation process especially involving transformations between the frames of reference

In addition to the work listed above, the following changes were also needed

a. Find and correct errors in the abrasion process concerning transformation of the laboratory angles of particles from the projectile and target
b. Extend the current UBERNSPEC calculations to mass numbers of the projectile and target nuclei beyond 68

c. Incorporate different p_0 values into the coalescence portion of the code and extend it to calculate secondary neutron and light ion cross sections with these p_0 values

4.3.1. Modifications in coalescence subprogram

The main program in the UBERNSPEC code contains an operational CALL statement which requests specific values from the subroutine COAL; in this particular case the values of double differential and Lorentz invariant cross sections for light ion production are returned. The subprogram COAL calculates these total cross sections for secondary neutron production, as well as the production of *deuterons, tritons, helions, and alphas* in energy and angular distributions using the coalescence formalism described in Chapter 2. This is a new development that differs from the previous work by Braley and collaborators [11]. The original subroutine COAL was completely reformulated to include the contribution from α production. In the previous version of the COAL subprogram, incorporating alpha production into the calculations would have required using complex arithmetic to obtain triple differential cross section, which was not done. To correct these shortcomings and improve the accuracy of the predictions, the expressions (47) and (48) were introduced to the COAL subroutine, and the program was reformulated into a new subroutine, which did not require the use of complex arithmetic. Unlike the previous version of the subroutine, which only estimated the effect of coalescence on the neutron distributions, the current COAL subprogram is also now capable of calculating light ion yields with energy and angular distributions and presents them in terms of double differential and Lorentz invariant cross sections. The revised COAL subprogram is shown in detail in Appendix B.1.

Another modification in the COAL subroutine is the extension of light ion cross section calculations using different critical radii of the momentum coalesced sphere p_0 values that were reported in several studies [1; 60; 62; 72; 79]. The critical radius p_0 value appeared in eq. (48) is an adjustable parameter obtaining by extracting the specific values from each experimental reaction. Table 4.1 lists suggested p_0 values for light ion calculations in high energy fragmentation interactions. In the original UBERNSPEC work, the p_0 value of 90 MeV/c reported in Nagamiya et al. [79] was used. In this work, the values reported by Awes and collaborators [1] and by Gutbrod and collaborators [62] are also used for the calculations; the resultant comparisons are illustrated in the next chapter. The detailed coding for different p_0 values is described in subroutine COAL listed in Appendix B.1

Authors	d (MeV/c)	t (MeV/c)	h (MeV/c)	α (MeV/c)
Gutbrod et al. 1976	129	129	129	142
Nagamiya et al. 1981	90	90	90	90
Awes et al. 1981	170	215	215	270

Table 4.1: The published experimental values of critical radius p_0 (MeV/c) of momentum sphere in coalescence volumes from various works are used for comparisons in this work.

4.3.2. Modifications in mass subprograms

The UBERNSPEC code was initially able to perform calculations of secondary neutron production for projectile and target nuclei that have mass numbers up to 68. The current code extended to compute cross sections of higher mass particles up to 238. To accomplish this, modifications of several subroutines and function modules, such as expanding the mass table in the AMASS function subprogram and expanding boundaries of some array variables in numerous function and subroutine subprograms were made. For the sake of simplicity in the actual UBERNSPEC program, an external mass table file was constructed and the mass data extracted by an OPEN statement in the AMASS function. Appendix B.2 shows the details of coding in the AMASS function and B.4

shows the mass table input data for the AMASS function.

Not only were the mass table and array boundaries extended to successfully complete the mass number expansion process, additional values of skin thickness and half density radius parameters were also needed. The values of these two parameters listed in the AWSPAR subroutine are parameterized as a function of mass number. The parameterized functions for estimating skin thickness and half density radius are shown in Figures 4.2 and 4.3, respectively. The AWSPAR subprogram is called by the AFORMWS subroutine (see Figure 4.1.b), which performs a parameterization of the nuclear charged density distributions using a two-parameter Fermi or Woods-Saxon function. This work follows the two-parameter Fermi formulation described in Maung et al. [75] and uses the tabulated charge and density distribution parameters for elastic scattering presented in De Jager et al. [35]. The detailed values of these two parameters listed in the AWSPAR subroutine are presented in Appendix B.3

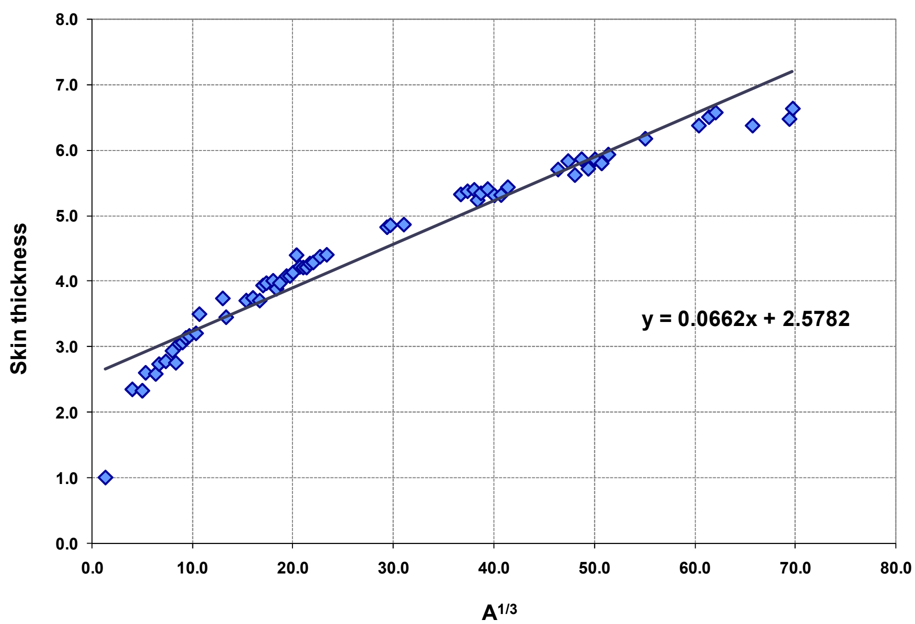

Figure 4.2: Skin thickness values in fm as a function of mass number.

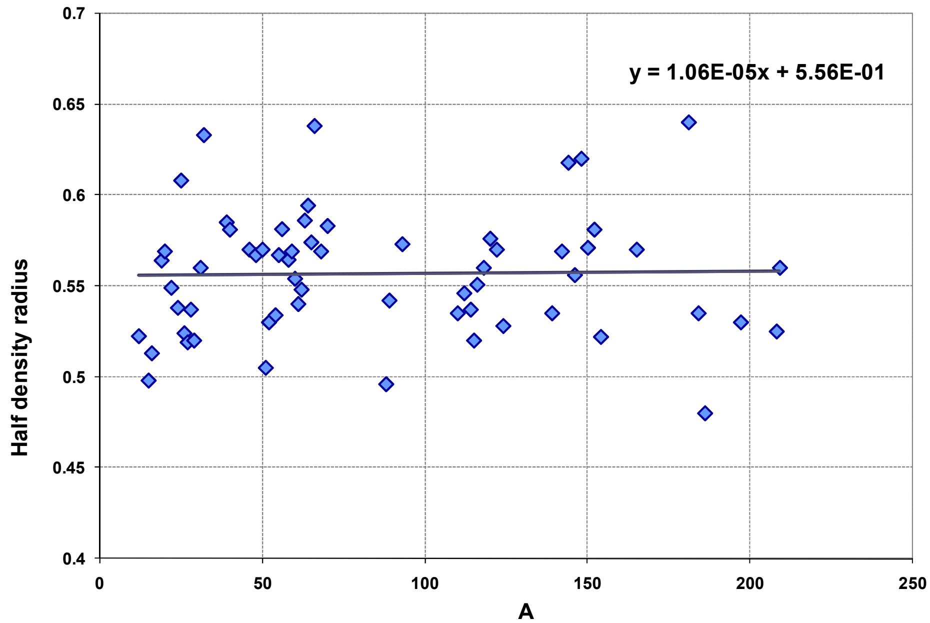

Figure 4.3: Half density radius values in fm as a function of mass number.

4.3.3. Modifications in coding errors

4.3.3.1. Reference rest frame transformation corrections

In general, the evaluation of the scattering interaction takes place in the reference rest frame of the nucleus that undergoes the fragmentation reaction. In the ideal situation, it is assumed that this is the projectile, since most cross sections were measured and reported in the laboratory reference frame. In previous work, target fragmentation was calculated simply by interchanging the projectile and target nuclei. The previous version of UBERNSPEC [11] calculated the ablation stage in the target by swapping the projectile and target in the NSPEC subroutine. It was discovered during the course of the present work, that the target spectra, rather than being calculated in the laboratory, were actually calculated in a reference frame where the target was moving in the laboratory with the projectile velocity. While attempting to modify the NSPEC coding to correct this error, it became obvious that modifying NSPEC to handle both cases was more straightforward and easily accomplished if the subroutine was revised to handle each case in separate versions, by dividing the NSPEC subroutine into a version for the projectile (NSPECPROJ) and a separate version (NSPECTAR) for the target (see Figure 4.1.a).

4.3.3.2. Issue of improper behavior at intermediate angles

Another issue discovered during the reformulation of the UBERNSPEC code is the improper behavior of energy dependent secondary neutron distributions at angles away from the incident beam direction (the intermediate angles). To illustrate this strange behavior, representative plots of total cross sections and abraded neutron cross sections from each contribution: projectile and target are shown in Figures 4.4 - 4.6, respectively. As seen in Figure 4.4, predictions of secondary neutron production cross sections at broad angles in the laboratory frame have similar energy distribution shapes as the measurements at small forward emission angles. Once the emission angle increases, the peak of the predicted secondary neutron spectra moves toward higher beam energies, rather than decreasing, causing the total neutron differential cross sections to be significantly overestimated. These behaviors are obviously incorrect, as can be seen from comparisons with the behaviors of typical experimental data at broad angles.

One attempt to resolve this issue involved separately calculating contributions of the projectile and contributions from the target. The subprograms responsible for performing these calculations are ABRKO and INQE. In the INQE subroutine, inclusive neutron momentum distributions from the knockout process are calculated, and these values are requested by the ABRKO subroutine and transformed into the proper forward directions. In this work, the ABRKO and INQE subprograms were broken up into two parts for calculations of abraded neutron spectra from contributions of projectile and target. The reason behind this was an attempt to indicate the effects of projectile and target nucleons on the knockout process in order to determine which of these lead to the improper behavior of the cross sections at the intermediate angles. Clearly as illustrated in Figures 4.5 and 4.6, the projectile contributions dominate the emitted neutron spectral distributions and lead to over-prediction of secondary neutron productions at high

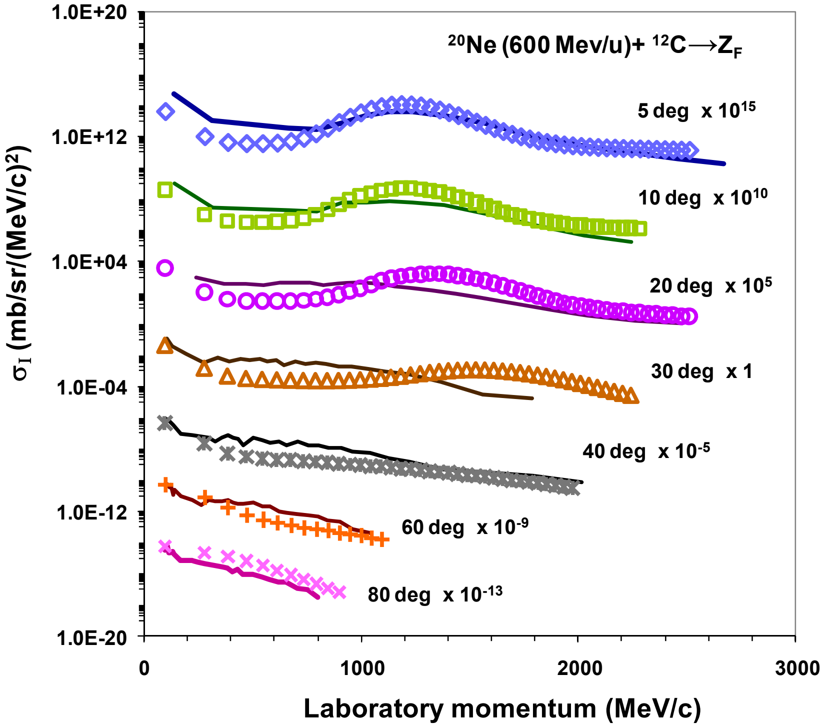

Figure 4.4: Distributions of Lorentz invariant cross sections for total secondary neutron at various laboratory angles for 600 MeV/nucleon ^{20}Ne + ^{12}C reactions. Line plots represent the experimental data and symbols represent the calculations from the ABRKO and INQE subprograms after separating the contributions of projectile and target. For display purposes, both measurements [80] and calculations are multiplied by multiplication factors of $10^{-13} - 10^{15}$.

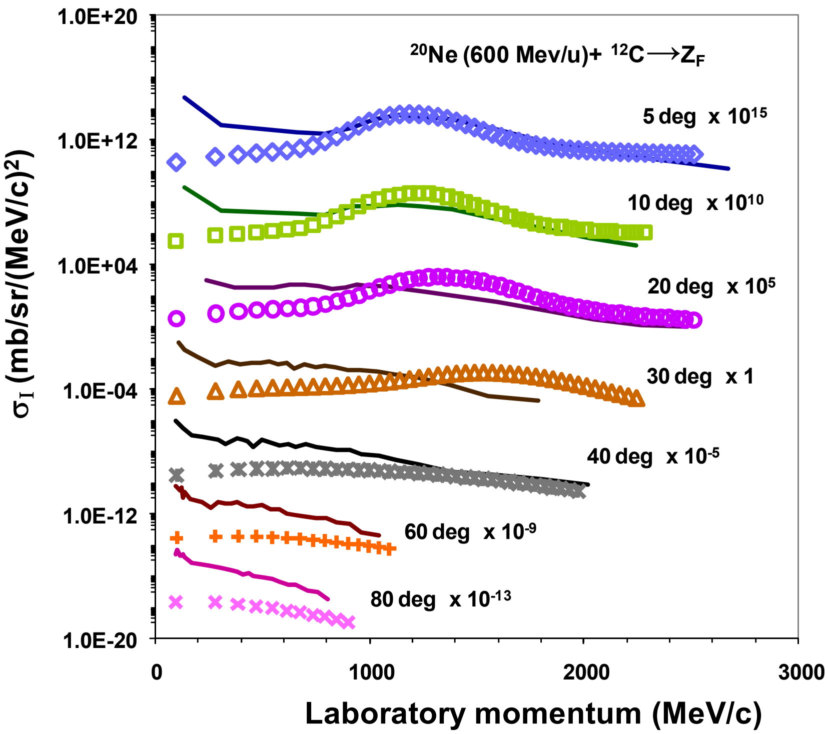

Figure 4.5: Distributions of Lorentz invariant cross sections for abraded neutron spectra from projectile contributions at various laboratory angles for 600 MeV/nucleon ^{20}Ne + ^{12}C reactions. Line plots represent the experimental data and symbols represent the calculations from the corresponding ABRKO and INQE subprograms. For display purposes, both measurements [80] and calculations are multiplied by multiplication factors of $10^{-13} – 10^{15}$.

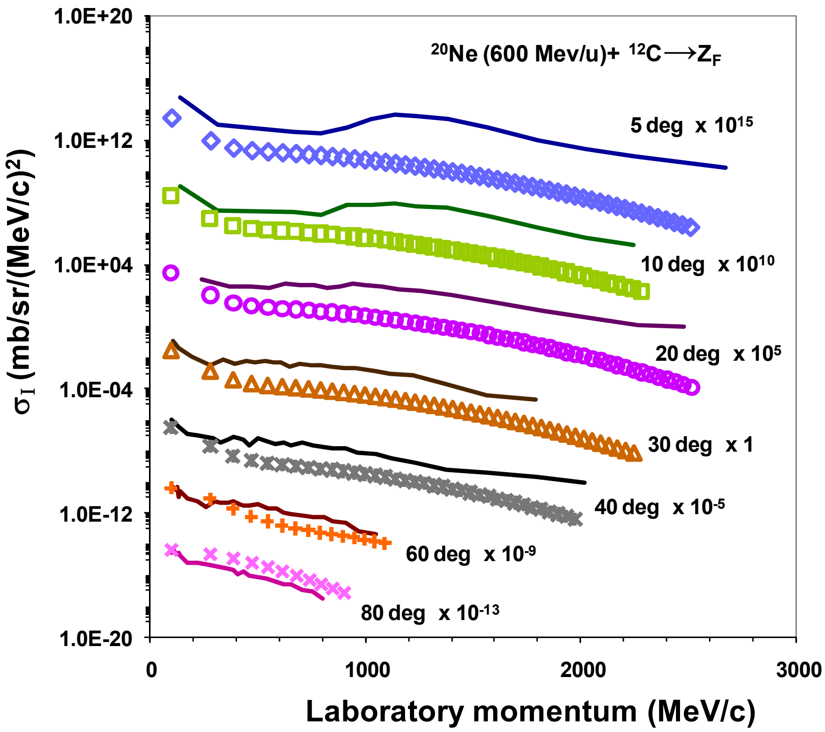

Figure 4.6: Distributions of Lorentz invariant cross sections for abraded neutron spectra from target contributions at various laboratory angles for 600 MeV/nucleon ^{20}Ne + ^{12}C reactions. Line plots represent the experimental data and symbols represent the calculations from the corresponding ABRKO and INQE subprograms. For display purposes, both measurements [80] and calculations are multiplied by multiplication factors of 10^{-13} – 10^{15}.

energies in the intermediate angles. In these two figures, lines represent the measurements from HIMAC accelerator experiment [80] and symbols are calculated secondary neutron spectra from either contributions of projectile or target in the corresponding ABRKO and INQE subprograms. To verify the changes in the calculated results from the combined ARBKO and from separate (projectile and target) ABRKO subprograms, the plot of secondary neutron spectra at 5º, 30º, 80º laboratory forward beam angles for the same reactions is displayed in Figure 4.7. Note that although the separation of the ABRKO and INQE subroutines (for projectile and target) yields no change in resultant cross sections, it helps to simplify the coding and to understand better the algorithm in the program. Similar results in different reactions are shown in Appendix C.1.

Since the incorrect behavior of the predicted neutron spectra at intermediate angles does not appear to be the result of coding errors, the likely explanation for the odd behavior of secondary neutron spectra at intermediate angle involves the fundamental formalism applied in the original work by Cucinotta et al. [26]. In the initial derivation of the underlying nuclear collision formalism developed by Cucinotta [18], a small angle approximation was introduced to the optical potential series for elastic scattering process at high energy in order to simplify the expansion by reducing some off-diagonal terms. The author further applied the small angle approximation to the scattering amplitude by assuming a small longitudinal momentum transfer which results in [18]

$$\mathbf{q} \cdot \mathbf{x} \approx \mathbf{q} \cdot \mathbf{b} + O(\theta^2) \tag{49}$$

where θ is the scattering angle which is assumed to be small. As a result, the expression of the scattering amplitude and the phase shift function reduced to eq. (7) and (10) presented in Chapter 2. This approximation has been embedded in the coding of the algorithm in the UBERNSPEC program. Reformulation of this approximation is considered to be beyond the scope of the present work, since it would involve reformulation the theory and completely reprogramming the knockout formalism in the UBERNSPEC code.

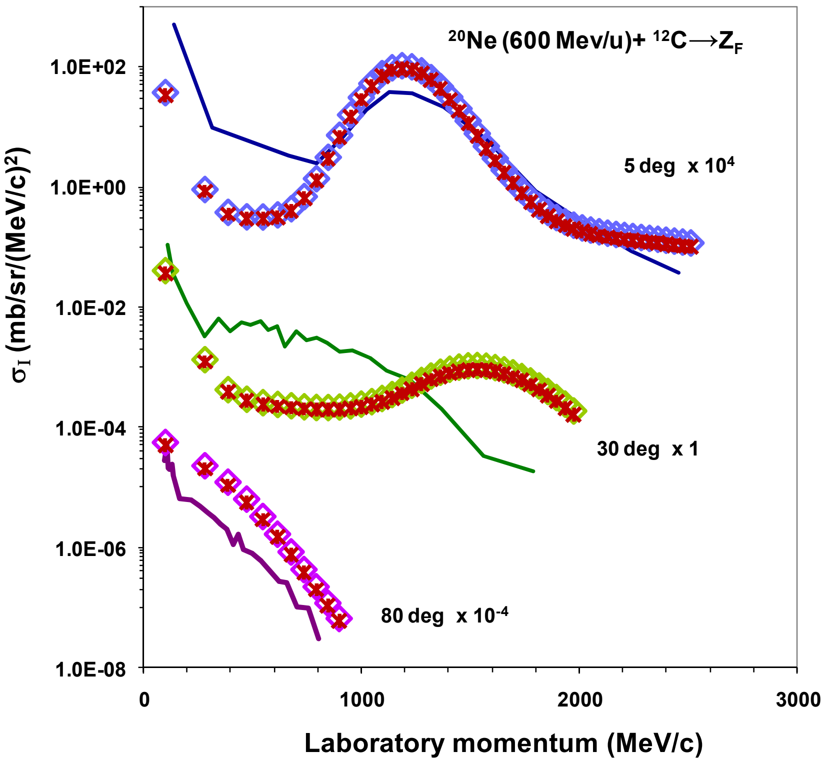

Figure 4.7: Distributions of Lorentz invariant cross sections for total neutron spectra at 5º, 30º and 80º laboratory angles for 600 MeV/nucleon ^{20}Ne + ^{12}C reactions. Line plots represent the experimental data, diamonds represent the calculations from the combined ABRKO and INQE subprograms, and asterisks are the calculations from separate contributions of projectile and target in ABRKO and INQE subprograms. For display purposes, both measurements [80] and calculations are multiplied by multiplication factors of $10^{-4} – 10^{4}$.

5. UBERNSPEC SAMPLE RESULTS

The purpose of these comparisons is to facilitate the discussion and to examine the accuracy of the UBERNSPEC calculations with some benchmark experimental data. Currently, the available published data used in this work are from Nakamura and Heilbronn [80], including experimental results from these accelerators: HIMAC, BEVALAC and RIKEN and from the BEVALAC experiments reported in Papp [84] As mentioned previously, the calculated cross sections from the UBERNSPEC code are expressed in the form of double differential spectral and angular yields or Lorentz invariant distributions, both in the laboratory reference rest frame. To convert from double differential cross sections to Lorentz invariant distributions, the inverse expression exhibited in eq. (46) is used. Typical results obtained from the UBERNSPEC code, presented in the following subsections, include plots of double differential and Lorentz invariant cross sections.

5.1. Secondary neutron productions

Representative comparisons of secondary neutron productions are made for the following reactions:

1. 135 MeV/nucleon ^{20}Ne beam colliding with a ^{207}Pb target
2. 337 MeV/nucleon ^{20}Ne beam colliding with a ^{238}U target
3. 390 MeV/nucleon ^{20}Ne beam colliding with a NaF target
4. 400 MeV/nucleon ^{40}Ar beam colliding with a ^{12}C target
5. 400 MeV/nucleon ^{131}Xe beam colliding with a ^{207}Pb target, and
6. 600 MeV/nucleon ^{20}Ne beam colliding with a ^{12}C target.

These neutron distributions are calculated at various laboratory angles, between 5° to 110°. The plots of Lorentz invariant cross section distributions are included in this section as well.

5.1.1. Reformulation of coalescence subprogram

5.1.1.1. Incorporation of α production contribution

After reformulation of the COAL subroutine in the UBERNSPEC code, a series of calculations for secondary neutron production and light ion production cross sections for various reactions were generated and compared with the measurements. One of the sample calculations is the secondary neutron spectra from the reaction of 390 MeV/nucleon neon beams colliding with a NaF nucleus target. The experimental neutron spectral distribution is from the work of Madey et al [73] as seen in Figure 5.1. The comparison shows fairly good agreement between the calculations of the current code with the measurements, especially at the peak of the beam energy. The current code, however, shows some slight disagreement with the measured neutron spectra at higher energies. The secondary neutron spectra with and without coalescence effects are displayed in Figure 5.2, as well as the measurements from [89]. Again, the comparison shows that the current UBERNSPEC code produces slightly better predictions of the secondary neutron cross sections particularly at the peak near beam energies, but tends to slightly overestimate distributions at higher energies. The discrepancy at energies well below the beam energy is primarily due to the neglect of the isobar formation and decay channel in the current formalism. Including the isobar channel is beyond the scope of the present work.

5.1.1.2. Development of Lorentz invariant cross sections

The reformulation of the coalescence subprogram also included formulating Lorentz invariant cross sections in addition to double differential cross sections. The capability of estimating cross sections using these two forms is necessary for the purpose of facilitating the estimating of cross sections in different reference frames, and comparing them with experimental data presented in those frames. Figure 5.3 displays overall momentum distributions (double differential and Lorentz invariant cross sections) compared to measurements reported by [80] for ^{40}Ar colliding with a ^{12}C target. Note

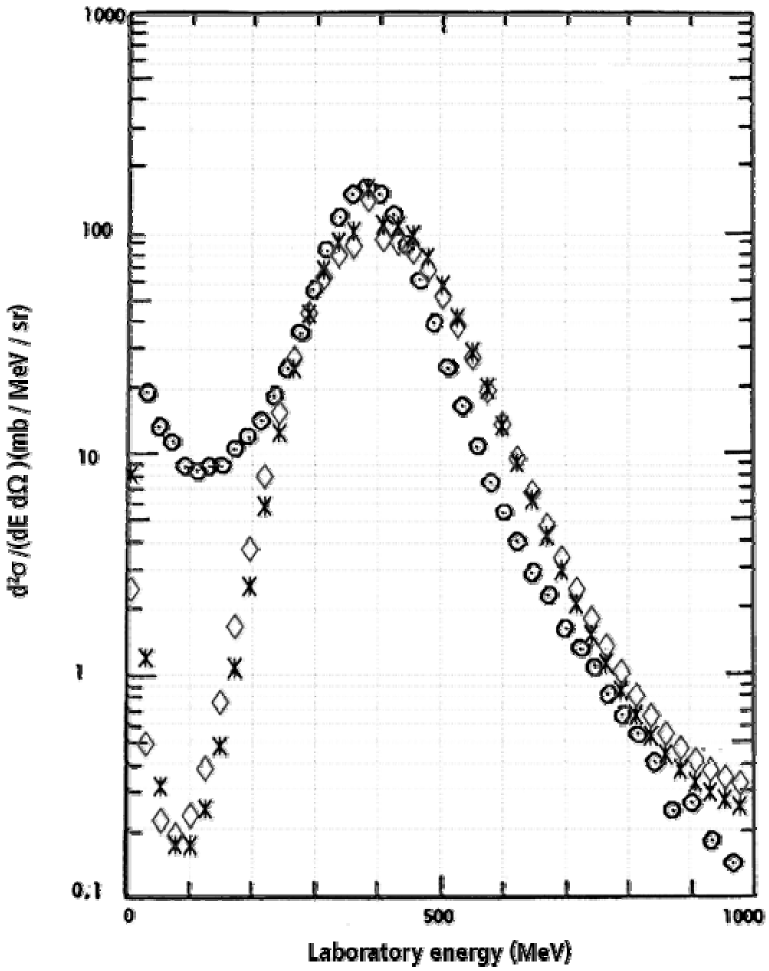

Figure 5.1: Comparison of predicted double differential neutron cross sections and energy spectra with measurements for 390A MeV Ne + NaF reactions at 0° in the laboratory. The open circles represent experimental data [73]; the diamonds are calculations with the coalescence effects from the previously modified UBERNSPEC code by [26]; and the asterisks are calculations with the coalescence effects from the current code.

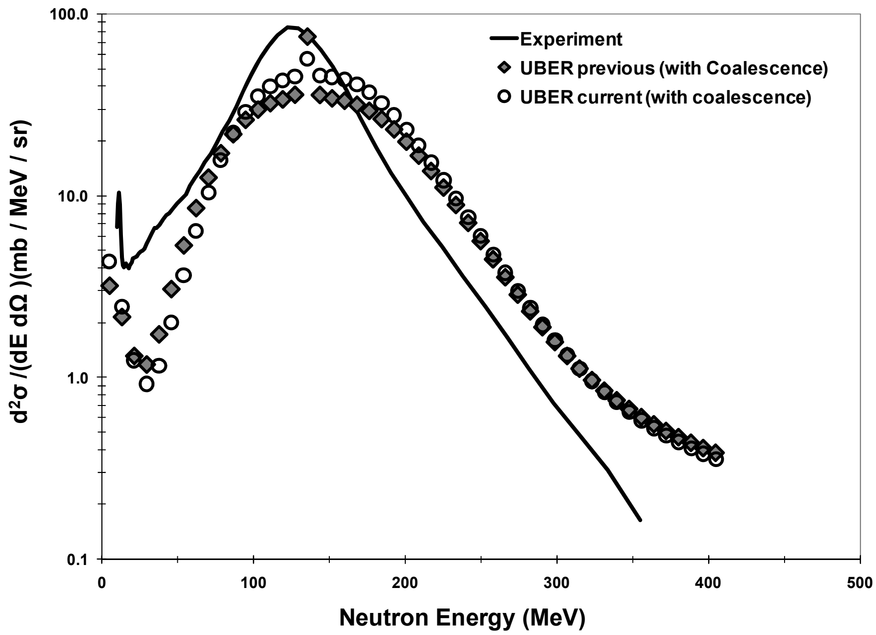

Figure 5.2: Comparison of predicted double differential neutron production cross sections and energy spectra with measurements for 135A MeV ^{12}C + ^{12}C reaction at 0° in the laboratory. The solid line represents experimental data [89]; the diamonds are calculations with the coalescence effects from the previously modified UBERNSPEC code by [26]; and the open circles are calculations with the coalescence effects from the currently modified UBERNSPEC code.

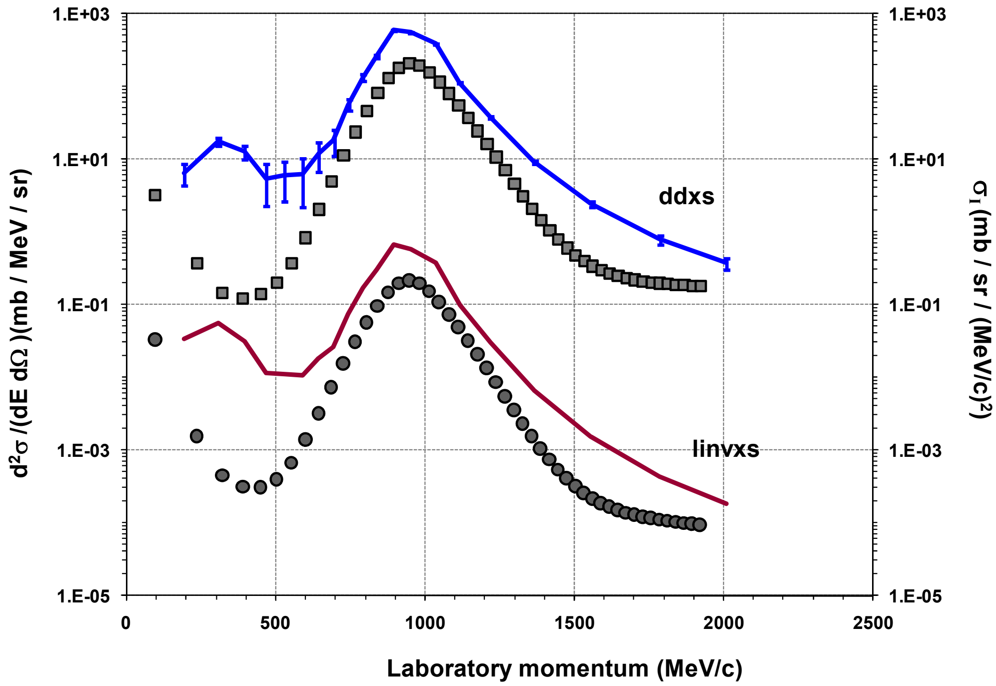

Figure 5.3: Secondary neutron spectra at 5º laboratory angle for the reaction of 400 MeV/nucleon ^{40}Ar colliding with ^{12}C target compares with published measured data [80] as shown in solid lines; the blue represents double differential cross sections (ddxs) and red represents Lorentz invariant cross sections (linvxs). The calculations are represented by filled squares for double differential cross sections and filled circles for Lorentz invariant cross sections.

that the significant discrepancy between these two figures below the beam energy is probably due to the need to incorporate neutrons produced by isobar formation and decay. More extensive studies on these topics are presented elsewhere [36, 95]. The incorporation of isobar production and decay channels will be included in future work.

5.1.2. Extensions of mass number applicability

As mentioned previously, the main modifications for extending the UBERNSPEC coding ability to handle mass numbers greater than 68 included: (1) extending the mass table in the AMASS subroutine and making of a mass data file, and (2) extending array boundaries and ranges of the nuclear skin thickness and half density radius parameters. Figure 5.4 shows a sample calculation of secondary neutron production in term of Lorentz invariant cross sections at 5º laboratory beam angle for the collision of 400 MeV/nucleon ^{131}Xe onto a ^{207}Pb target. In general, the UBERNSPEC code fairly good agreement with the measurements, especially for the shape of the distributions. However, there is some disagreement in the magnitudes of the cross sections. Figure 5.4 not only displays the total Lorentz invariant cross sections for secondary neutron, but it include the separate contributions from the projectile, target and their sums from knockout and ablation processes. The discussions of their effects are presented in subsequent sections. More of these sample calculations for various beam angles in the forward direction are shown in Appendix C.1.

Figure 5.5 displays secondary neutron spectra at 30º laboratory angle for the interaction of ^{20}Ne at 337 MeV/nucleon beam energy colliding with a ^{238}U target. Unlike the secondary neutron spectrum in Figure 5.4, which is dominated by the contribution from the ablation process, the secondary neutron spectral distribution from the neon and uranium interaction in Figure 5.5 is dominated by the contribution from the knockout process. One simple explanation is that when both nuclei are heavy, the spectator piece (prefragment) has more nucleons in it and more excitation energy meaning that more nucleons are emitted in the ablation process. On the other hand, when a projectile with

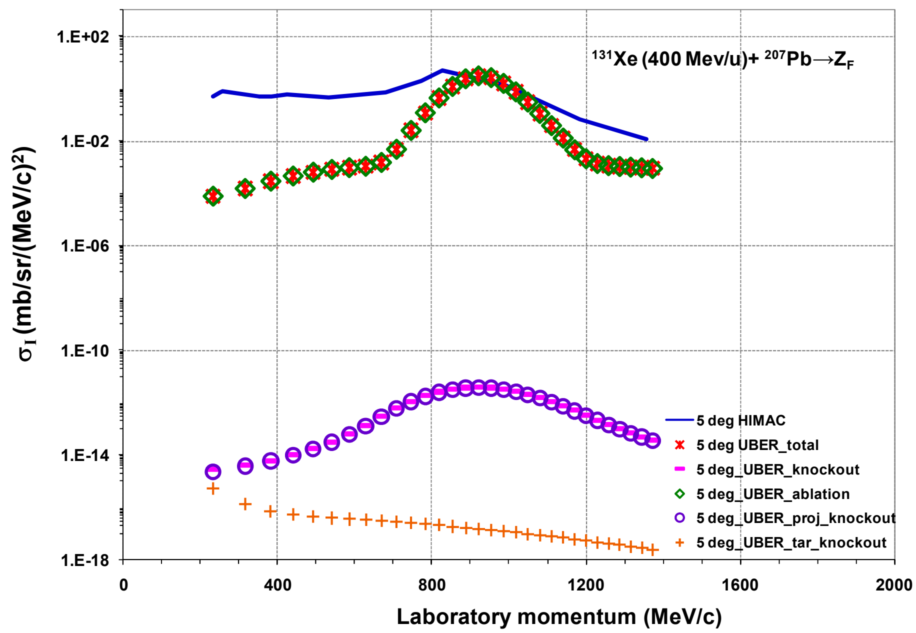

Figure 5.4: Secondary neutron spectra at 5º laboratory angle for the reaction of 400 MeV/nucleon ^{131}Xe colliding with a ^{207}Pb target compared with published measured data [80]. Separate contributions from the knockout stage (dash lines), the ablation stage (diamonds), and their sums (asterisks) are indicated for the calculations. The contributions of projectile (open circles) and target (plus symbols) from knockout processes are also explicitly displayed for the calculated results.

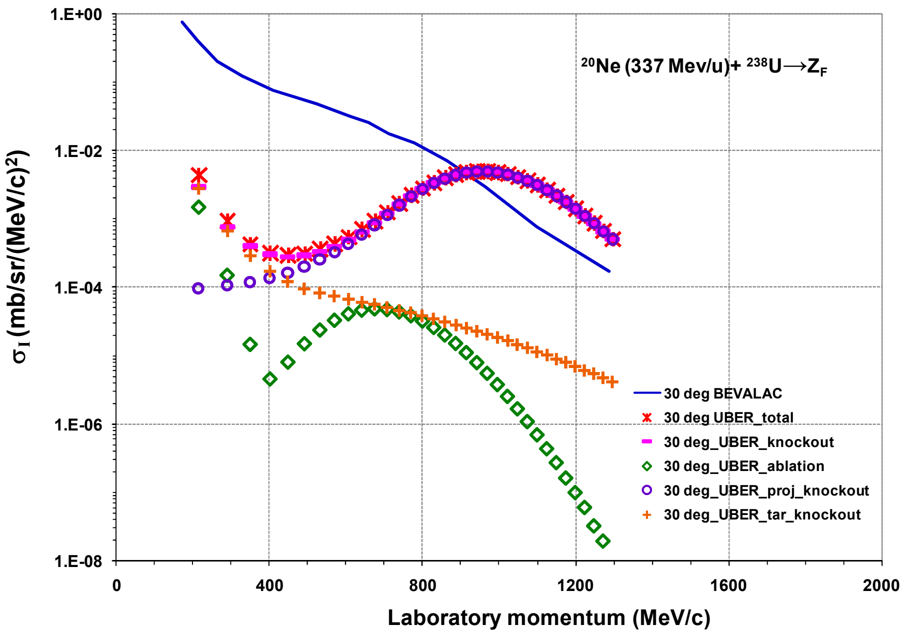

Figure 5.5: Secondary neutron spectral distribution for the reaction of 337 MeV/nucleon ^{20}Ne colliding with a ^{238}U target at 30^o laboratory angle compared with published measured data [80] as shown in the solid line. Separate contributions from knockout stage (dash lines), ablation stage (diamonds), and their sums (asterisks) for the calculations are also displayed. The contributions of projectile (open circles) and target (plus symbols) from the knockout process are also explicitly displayed for the calculated results.

less mass interacts with the heavy stationary target, the prefragment has a lower mass number and excitation energy and therefore ablates fewer nucleons. Therefore, the momentum distribution of neutrons produced in the knockout stage dominates the neutron spectrum.

Note that there are disagreements between distributions produced by the calculations and measurements as the laboratory angles increase. To demonstrate the breakdown between the theoretical and experimental data, Figures 5.6 and 5.7 compare a series of calculated neutron spectral distributions from previously mentioned reactions at different forward laboratory beam angles with the measurements reported in [80]. In general, the calculations show a fairly good agreement in the overall shape of neutron momentum distributions with the experimental data at small forward beam angles, but they tend to underestimate the predictions when the beam angles become larger. This probably results from small angle approximations and assumptions applied in the original theoretical work. Once again, the discrepancy below the beam energy is mainly caused by the lack of isobar formation and decay in the present work.

5.1.3. Improvements in the UBERNSPEC algorithm coding

5.1.3.1. Reference frame transformation modifications

Recall from Chapter 4 that modifications to the code were made to correct frame transformation issues, particularly for the NSREC and ABRKO subprograms. In order to illustrate the improvement in the predictions of secondary neutron production as a result of splitting NSPEC into separate subroutines for the projectile and target, a series of comparisons is made and shown in the following figures. Figure 5.8 shows a comparison of secondary neutron momentum distributions before the modifications in the NSPEC subprogram. Note that the contribution from the target clearly has the incorrect energy distribution since it is centered about the beam momentum. Figure 5.9 shows the calculations **after** the modifications in the NSPEC subprogram. Note that the contribution from the target now appears to have the proper momentum distribution,

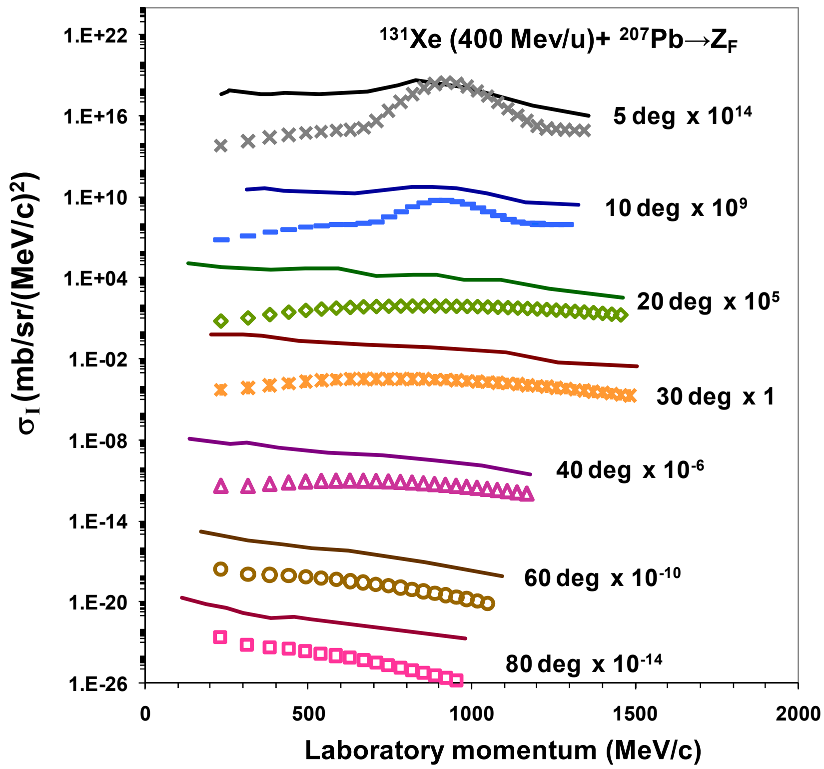

Figure 5.6: Secondary neutron spectral distributions produced by the current UBERNSPEC code for 400 MeV/nucleon ^{131}Xe colliding with ^{207}Pb target at various laboratory forward beam angles compared with published measured data [80]. Solid lines represent the experimental data and symbols represent calculated neutron spectral distributions.

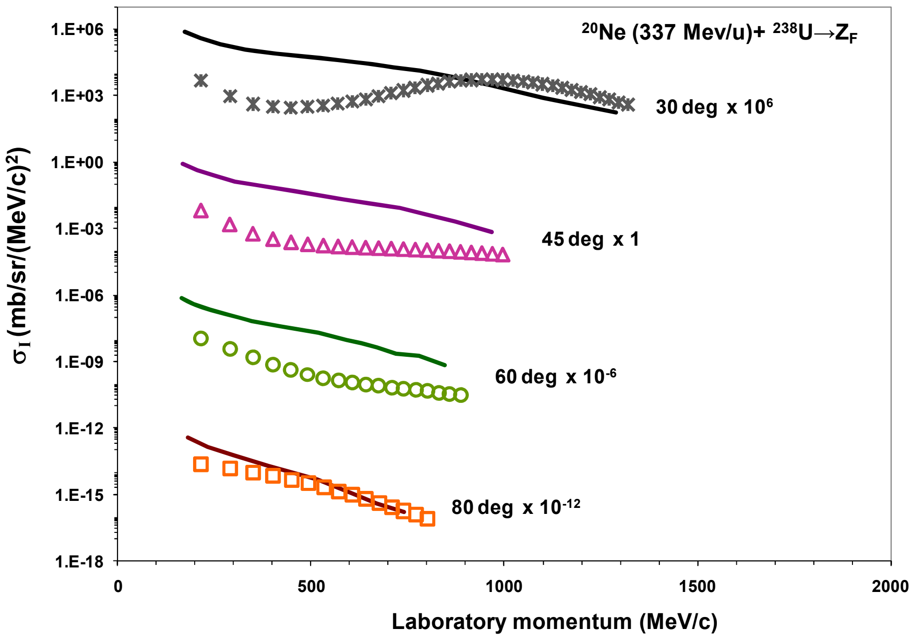

Figure 5.7: Secondary neutron spectral distributions produced by the current UBERNSPEC code for 337 MeV/nucleon ^{20}Ne colliding with a ^{238}U target at various laboratory forward beam angles compared with published measured data [80]. Solid lines represent the experimental data and symbols represent the neutron spectral distributions.

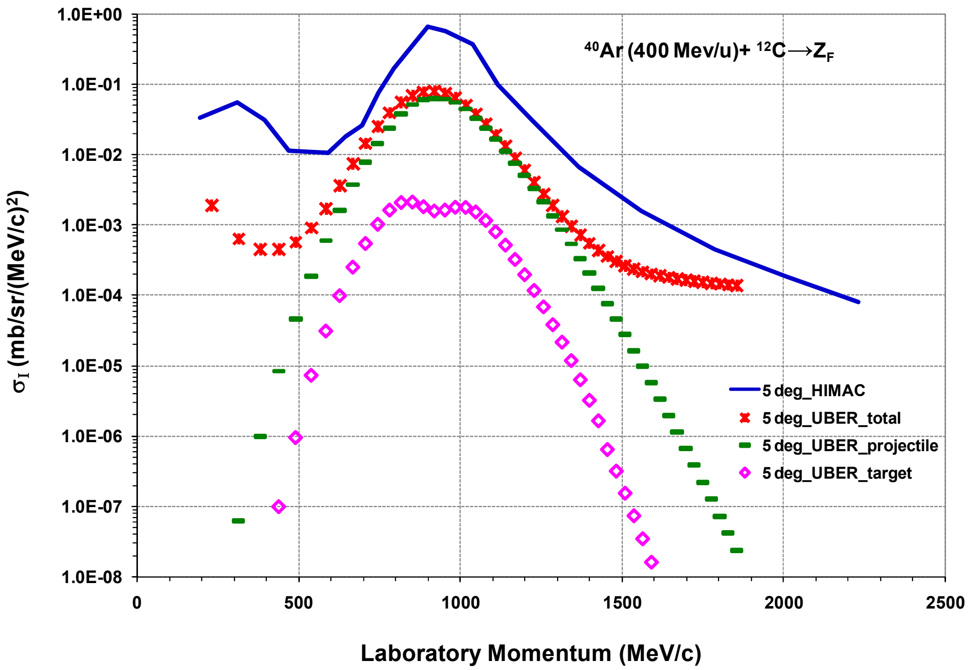

Figure 5.8: Secondary neutron Lorentz-invariant cross sections at 5° laboratory angle from the reaction of 400 MeV/nucleon ^{40}Ar colliding with ^{12}C target compared with published measured data represented a by solid line [80]. The calculation was based on the UBERNSPEC code before the current modifications in the NSPEC subprogram. Separate contributions of projectile (dash lines) and target (open circles) from ablation process and their total (from knockout and ablation stages) as shown using asterisks are explicitly displayed for the calculated results.

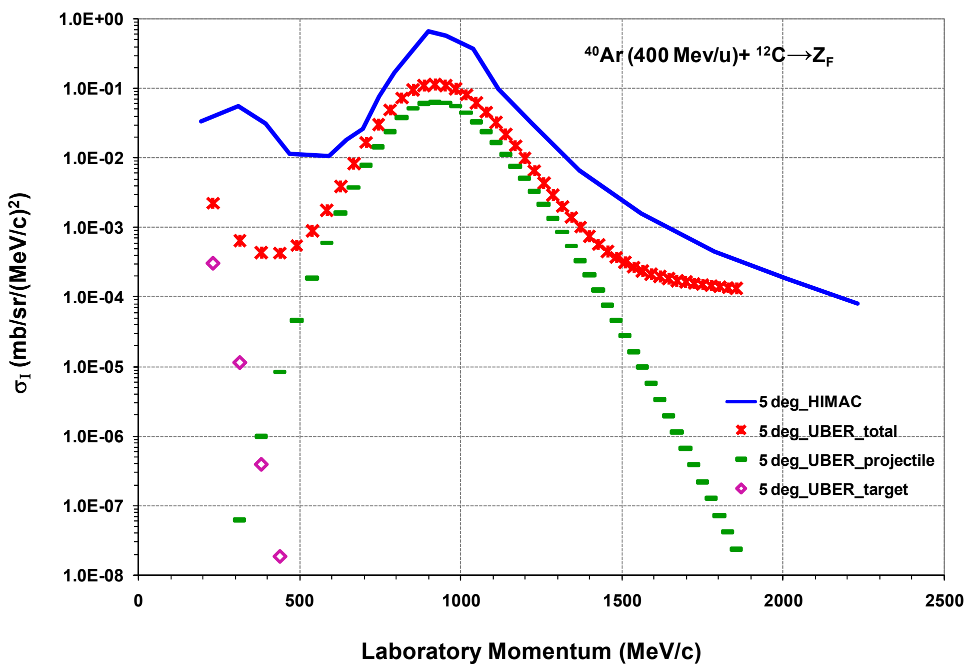

Figure 5.9: Secondary neutron production Lorentz-invariant cross sections at 5º laboratory angle from the reaction of 400 MeV/nucleon ^{40}Ar colliding with ^{12}C target compared with published measured data [80] represented by a solid line. The calculation was based on the UBERNSPEC code after the current modification in NSPEC subprogram. Separate contributions of projectile (dash lines) and target (open circles) neutrons from the ablation process and their total sum (from knockout and ablation stages) as shown using asterisks are explicitly displayed for the calculated results.

since it is a maximum at zero momentum (target at rest) and decreasing with increasing momentum a behavior that is expected since the neutron spectra from the target are mainly low energy particles that have evaporated from a source that is moving slowly in the laboratory. Lastly Figure 5.10 shows the calculations **after** modification to both the NSPEC and ABRKO subprograms. As expected, the improvement in the predictions (strong agreement with the measurements) can be obtained by using the current code.

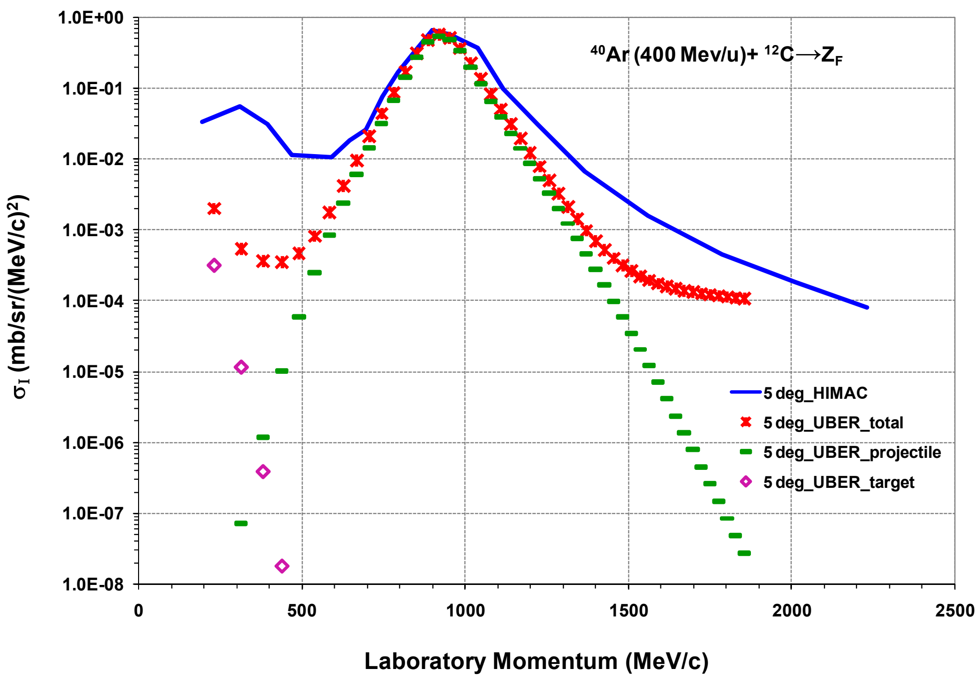

Figure 5.10: Secondary neutron Lorentz-invariant cross sections at 5° laboratory angle from the reaction of 400 MeV/nucleon ^{40}Ar colliding with ^{12}C target compared with published measured data [80] represented by a solid line. The calculation was based on the current UBERNSPEC code after the modifications to both NSPEC and ABRKO subprograms. Separate contributions of projectile (dash lines) and target (open circles) neutrons from the ablation process and their total sum (from knockout and ablation stages) as shown using asterisks are explicitly displayed for the calculated results.

5.2. Light ion production

The interactions of heavy charged particles at high energies can also produce momentum distributions of light ions. For the first time, the ability of the current UBERNSPEC code to calculate light ion momentum distributions is illustrated in this section. The comparisons are based on available experimental data from Papp et al. [84]. These data are limited to small angles in the forward direction. Other reports on the measurements of *protons, deuterons, tritons, helions* and *alphas* from nuclear fragmentation interactions using different high-energy accelerators [4; 61; 65] are being mined for data and will be incorporated into future analyses.

5.2.1. Construction of light ion momentum distribution

Figure 5.11 shows representative calculated light ion Lorentz-invariant momentum distributions at 2.5º laboratory angle for the reaction of a 1.05 GeV/nucleon carbon beam colliding with a carbon target. Although there are only few measured data presented for comparisons, the general results show fairly good agreement especially for the spectrum near the beam momentum.

5.2.2. Extension of coalescence calculations to various p_0 values

The free parameter critical radius p_0 values were presented in Table 4.1; these values were derived from empirical analyses reported in various studies. Calculations based on parameterized p_0 values from Nagamiya et al. [79] and Awes et al. [1] are used and the light ion production cross section results compared with the measurements at 2.5° from Papp [84] for the reaction of 1.05 GeV/c/nucleon carbon colliding with carbon and copper targets, as shown in Figures 5.12 and 5.13, respectively. Note that the calculations based on Awes and collaborators' p_0 values potentially yield higher prediction cross sections of light ions than the ones that were used by Nagamiya and collaborators' [79] (Figure 5.12). The simple explanation for this behavior involves the constant *R(Z, n)* in eq. (48) where it is seen that the p_0 value in the expression is raised to the cubic power in terms of mass number. Hence, increasing in the critical radius values will cause the particle momentum distributions to become larger since there is a higher probability that coalescence will occur.

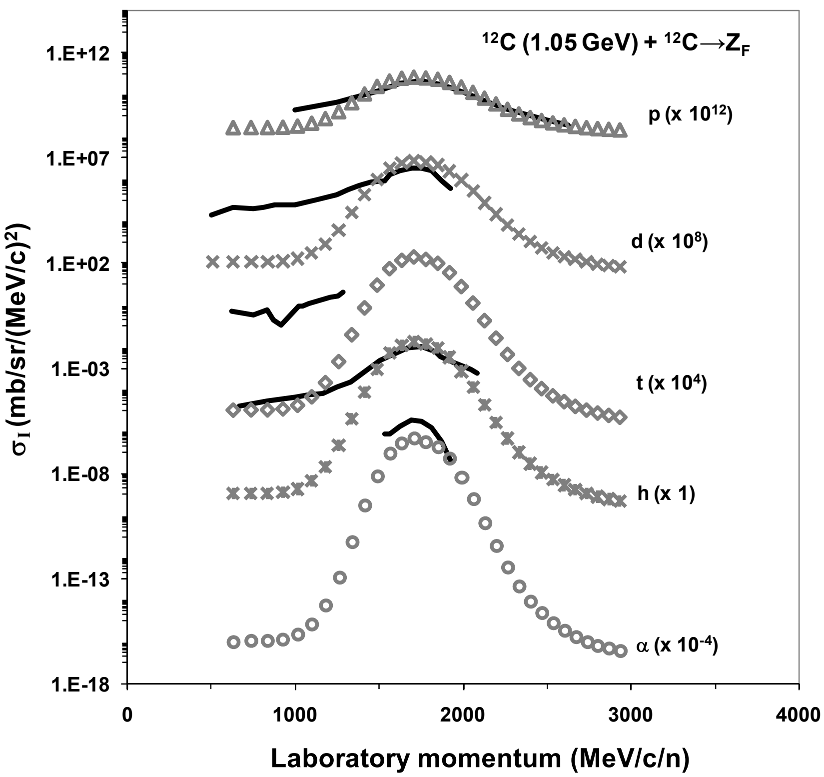

Figure 5.11: Lorentz invariant cross sections at 2.5° laboratory angle of ^{2}H(d), ^{2}He(t), ^{3}He(h) and ^{4}He(α) produced from the interaction of 1.05 GeV/nucleon ^{12}C colliding with a ^{12}C target compared with published measured data [84]. Solid lines are the experimental data, triangles are the proton spectral distribution, cross symbols are the deuteron spectral distribution, squares are the triton spectra, asterisks are the helion spectra, and open circles are the alpha distribution. Multiplication factors from 10^{12} – 10^{-4} were used to separate the curves for illustrative purposes.

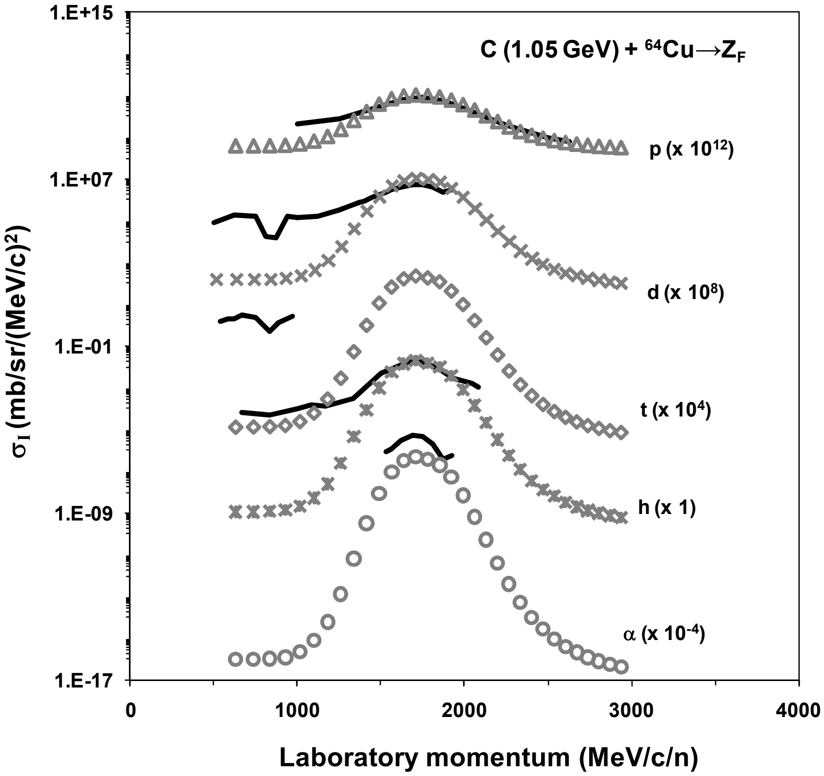

Figure 5.12: Lorentz invariant cross sections at 2.5º laboratory angle of light ion production for 1.05 GeV/nucleon ^{12}C colliding with a ^{64}Cu target compared with published measured data [84]. The calculations are based on the critical radius p_0 values suggested by Nagamiya et al. [79]. Solid lines are the experimental data, triangles are the proton spectral distribution, cross symbols are the deuteron spectral distribution, squares are the triton spectra, asterisks are the helion spectra, and open circles are the alpha distribution. Multiplication factors from 10^{12} – 10^{-4} were used to separate the curves for illustrative purposes.

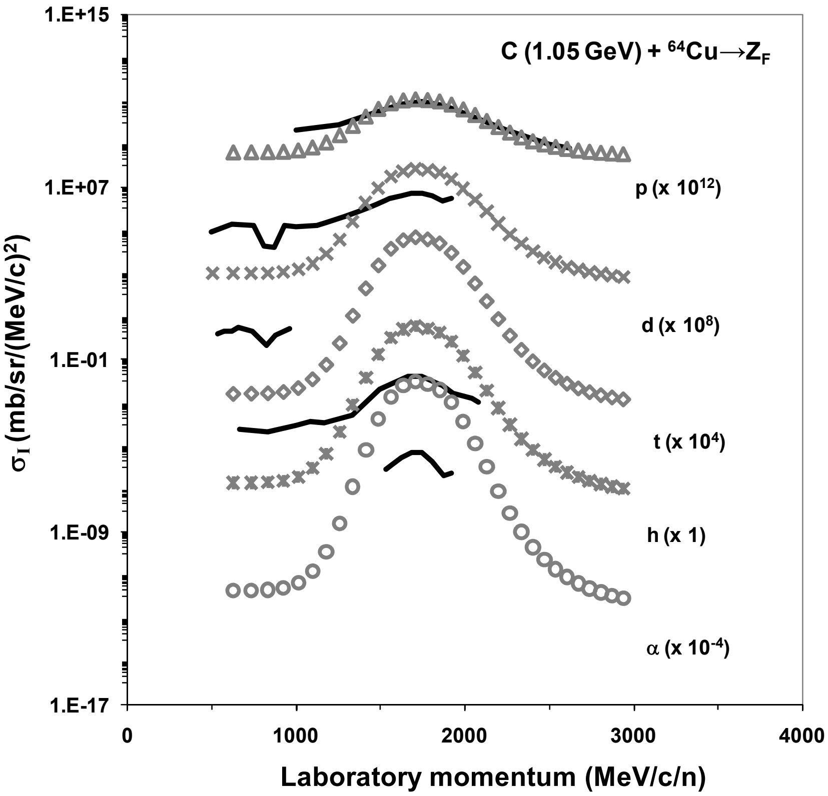

Figure 5.13: Lorentz invariant cross sections of light ion production at 2.5º laboratory angle for 1.05 GeV/nucleon ^{12}C colliding with a ^{64}Cu target compared with published measured data [84]. The calculation is based on the critical radius p_0 value suggested by Awes et al. [1]. Solid lines are the experimental data, triangles are the proton spectral distribution, cross symbols are the deuteron spectral distribution, squares are the triton spectra, asterisks are the helion spectra, and open circles are the alpha distribution. Multiplication factors from 10^{12} – 10^{-4} were used to separate the curves for illustrative purposes.

6. CONCLUSIONS AND FUTURE WORK

In the previous chapter, representative predictions using the current UBERNSPEC code were presented and compared with available experimental data. In this chapter, a summary of the UBERNSPEC reformulations, extensions, and other modifications are described and suggestions for future improvements included.

6.1. Result discussion and conclusion

In the present work, significant modifications to improve the UBERNSPEC code, including the extension of the coalescence formulation to incorporate the effects of α particle coalescence, extend the coalescence model to actually predict energy and angular distributions of light ions (deuterons, tritons, helions, and alphas) for the first time, and extending the capabilities of the code to predict secondary particle production cross sections for collisions involving nuclei that have mass numbers greater than 68 were made. To accomplish these tasks required

a. Reformulating the coalescence model in the code by developing the expressions based on Lorentz invariant cross sections rather than double differential cross sections.
b. Extending the code to include the contribution of α production in the coalesced volume.
c. Finding and correcting coding errors in the ablation process especially involving transformations between the frames of reference. This involved separating the NSPEC subprogram to separate subprograms for the projectile and target nuclei.

In addition to the work listed above, the following changes were also made

d. Finding and correcting errors in the abrasion process concerning transformation of the laboratory angles of particles from the projectile and target. This involved separating the ABRKO subprogram into separate entities for the projectile and target nuclei.

e. Extending the current UBERNSPEC calculations to mass numbers of the projectile and target nuclei greater than 68
f. Incorporate different p_0 values into the coalescence portion of the code and extend it to calculate secondary neutron and light ion cross sections with these p_0 values
g. Expand the comparison of results to additional published data especially for the light ion production.

In general there is improved agreement between UBERNSPEC predictions and measurements of neutron spectra for angles near the incident beam direction. Significant discrepancies still exist for neutron production at broader angles, which appear to result from the use of small angle assumptions and approximations in the underlying theoretical model. There is also disagreement at forward angles between model predictions and data for neutron energies several hundred MeV lower than the beam energy per nucleon resulting from the neglect of the nucleon isobar formation and decay channel. Correcting these shortcomings is an ambitious endeavor and is beyond the scope of the present work.

6.2. Suggested future work

The UBERNSPEC code is a work in progress. There are the needs for key improvements involving the physical theory underlying the present model. A few suggestions are:

1. Incorporate the isobar formation and decay channel. A more detailed description of isobar production and decay are presented in papers by Deutchman and Townsend [35; 94].
2. Correct the improper behavior of predicted neutrons spectra at intermediate angles

away from the forward beam direction. Due to the theoretical assumptions embedded in the original work, correcting this problem is an extensive undertaking since it requires reformulating the underlying theory and concomitantly involves very extensive re-coding of UBERNSPEC.

3. Expansion of the coding output format. Now that the current code can produce both double differential and Lorentz invariant cross sections, the future modified code should also include output in the form of differential cross sections and/or total fragment yields or cross sections. This will enable the calculations to compare with nuclear cross section data from other studies.

REFERENCES

1. Awes TC, Poggi G, Gelbke CK. 1981. Precompound emission of light particles in the reaction $^{16}O + {}^{238}U$ at 20 MeV/nucleon. Phys Rev C. 24(1):89-109.
2. Barth JL, Dyer CS, Stassinopoulos EG. 2003. Space, atmospheric and terrestrial radiation environments. IEEE Trans Nucl Sci. 50(3):466-482.
3. Benary O, Price LR, Alexander G. 1970. NN and ND interactions – a compilation. Lawrence Radiation Laboratory. Report No.: UCRL-20000NN. (Unpublished).
4. Bergenwall BE, Ataç A, Kullander S. 2005. Neutron-induced light charged particle production in carbon at 96 MeV. Nucl Phys A. 747:152-181.
5. Bertini HW. 1969. Intranuclear-cascade calculation of the secondary nucleon spectra from nucleon-nucleus interactions in the energy range 340 to 2900 MeV and comparisons with experiment. Phys Rev. 188(4):1711-1730.
6. Bethe HA. 1958. Scattering and polarization of protons by nuclei. Ann Phys. 3:190-240.
7. Bhasin VS, Verma VS. 1969. Corrections to the Glauber model of high-energy scattering. Phys Rev. 184(5):1338-1342.
8. Bleszynski M, Sander C. 1979. Geometrical aspects of high-energy peripheral nucleus-nucleus collisions. Nucl Phys A 326:525-535.
9. Bondorf JP, Fái G, Nielsen OB. 1978. Ground-state correlations observable in hard heavy-ion reactions. Phys Rev Lett. 41(6):391-394.
10. Bowman JD, Swiatecki WJ, Tsang CF. 1973. Abrasion and ablation of heavy ions. University of California. Report No.: LBL-2908.
11. Braley GS, Townsend LW, Cucinotta FA, Heilbronn LH. 2002. Modeling of secondary neutron production from space radiation interactions. IEEE Trans Nucl Sci. 49(6):2800-2804.
12. Britt HC, Quinton AR. 1961. Alpha particles and protons emitted in the bombardment of Au^{197} and Bi^{209} by C^{12}, N^{14}, and O^{16} projectiles. Phys Rev. 124(3):877-887.
13. Butler ST, Pearson CA. 1963. Deuterons from high-energy proton bombardment of matter. Phys Rev. 129(2):836-842.
14. Chamberlain O, Segrè E, Tripp RD, Wiegand C, Ypsilantis T. 1957. Experiments with 315-Mev polarized protons: proton-proton and proton-neutron scattering. Phys

Rev. 105(1):288-301.

15. Chew GF. 1950. The inelastic scattering of high energy neutrons by deuterons according to the impulse approximation. Phys Rev. 80(2):196-202.
16. Chew GF, Goldberger ML. 1952. The scattering of elementary particles by complex nuclei-A generalization of the impulse approximation. Phys Rev. 87(5):778-782.
17. Chew GF, Wick GC. 1952. The impulse approximation. Phys Rev. 85(4):636-642.
18. Cucinotta FA. 1988. Theory of alpha-nucleus collisions at high energies. [Ph D. Dissertation]. Norfolk (VA): Physics department. Old Dominion University. 89 p.
19. Cucinotta FA, Wilson JW, Townsend LW, Khandelwal GS. 1989. Corrections in α-α scattering and semi-classical optical models. Phys Lett B. 223(2):127-132.
20. Cucinotta FA, Wilson JW, Townsend LW. 1992A. Inclusive inelastic scattering of heavy ions in the independent particle model. J Phys G: Nucl Part Phys. 18:889-901.
21. Cucinotta FA, Wilson JW, Townsend LW. 1992B. Multiple-scattering effects in quasielastic α- ^{4}He scattering. Phys Rev C. 46(4):1451-1456.
22. Cucinotta FA, Dubey RR. 1993. Final state interactions and inclusive nuclear collisions. Springfield, VA: National Technical Information Service. Report No.: NASA TP-3353.
23. Cucinotta FA. 1994. Forward production of protons in relativistic ^{12}C-nucleus collisions. J Phys G: Nucl Part Phys. 20:1803-1815.
24. Cucinotta FA. 1994. Multiple-scattering model for inclusive proton production in heavy ion collisions. Springfield, VA: National Technical Information Service. Report No.: NASA TP-3470.
25. Cucinotta FA, Dubey RR. 1994. Alpha-cluster description of excitation energies in ^{12}C (^{12}C, 3α) X at 2.1A GeV. Phys Rev C. 50(2):1090-1096.
26. Cucinotta FA, Wilson JW, Townsend LW. 1997. Abrasion-ablation model for neutron production in heavy ion collisions. Nucl Phys A. 619:202-212.
27. Cucinotta FA, Wilson JW, Townsend LW, Tripathi RK. 1998. Microscopic fragmentation model for galactic cosmic ray studies. Adv Space Res. 22(4):533-537.
28. Cucinotta FA, Wilson JW, Saganti P, Hu X, Kim MY, Cleghorn T, Zeitlin C,

Tripathi RK. 2006. Isotopic dependence of GCR fluence behind shielding. Rad Meas. 41:1235-1249.

29. Cucinotta FA, Kim MH, Schneider SI, Hassler DM. 2007. Description of light ion production cross sections and fluxes on the Mars surface using the QMSFRG model. Radiat Env Biophys. 46:101-106.
30. Cugnon J. 1980. Monte Carlo calculation of high-energy heavy-ion interactions. Phys Rev C. 22(5):1885-1896.
31. Curtis SB, Doherty WR, Wilkinson MC. 1969. Study of radiation hazards to man on extended near earth missions. Springfield (VA): National Technical Information Service. Report No.: NASA CR-1469.
32. Curtis SB, Wilkinson MC. 1972. The heavy particle hazard –what physical data are needed?. *Proceeding of the national symposium on natural and manmade radiation in space*. EA Warman, ed. Springfield (VA): National Technical Information Service. Report No.: NASA TM X-2440. p 1007-1015.
33. Czyż W, Maximon LC. 1969. High energy, small angle elastic scattering of strongly interacting composite particles. Ann Phys. 52:59-121.
34. Dar A, Kirzon Z. 1971. Simple explanation of elastic scattering of heavy ions. Phys Lett B. 37(2):166-169.
35. De Jager CW, De Vries H, De Vries C. 1974. Nuclear charge- and magnetization-density-distribution parameters from elastic electron scattering. Atomic data and nuclear data tables. 14(5-6):479-508.
36. Deutchman PA, Townsend LW. 1980. Coherent isobar production in peripheral relativistic heavy-ion collisions. Phys Rev Lett. 45(20):1622-1625.
37. Dostrovsky I, Fraenkel Z, Friedlander G. 1959. Monte Carlo calculations of nuclear evaporation processes III applications to low-energy reactions. Phys Rev. 116(3):683-702.
38. Fäldt G, Pilkuhn H, Schlaile G. 1974. Nucleus-nucleus collisions at relativistic energies. Ann Phys. 82:326-344.
39. Feshbach H, Hüfner J. 1970. On scattering by nuclei at high energies. Ann Phys. 56:268-294.
40. Foldy LL. 1945. The multiple scattering of waves I. general theory of isotropic

scattering by randomly distributed scatterers. Phys Rev. 67(3):107-119

41. Foldy LL, Walecka JD. 1969. On the theory of the optical potential. Ann Phys. 54:447-504.
42. Franco V. 1966. Small-angle high-energy scattering by deuterons. Phys Rev Lett. 16(21):944-947.
43. Franco V, Glauber RJ. 1966. High-energy deuteron cross sections. Phys Rev. 142(4):1195-1214.
44. Franco V. 1968. High-energy nucleus-nucleus collisions I general theory and applications to deuteron-deuteron scattering. Phys Rev. 175(4): 1376-1393.
45. Franco V. 1976. High energy collisions between heavy nuclei. Phys Lett B. 61(5):444-448.
46. Franco V. 1976. Optical limits of the Glauber approximation for nucleus-nucleus collisions. Phys Lett B. 64(1):13-16.
47. Franco V, Nutt WT. 1977. Pauli correlations in heavy-ion collisions at high energies. Nucl Phys A. 292(2):506-522.
48. Franco V, Tekou A. 1977. High-energy heavy-ion scattering and the optical phase shift function. Phys Rev C. 16(2):658-644.
49. Franco V, Verma GK. 1977. Nucleus-nucleus scattering at high energies. Phys Rev C. 15(4):1375-1378.
50. Franco V, Nutt WT. 1978. Short range correlations in high energy heavy ion collisions. Phys Rev C. 17(4):1347-1358.
51. Friedberg W, Copeland K, Duke FE, Darden Jr EB, O'Brien III K. 1999. Guidelines and technical information provided by the US Federal Aviation Administration to promote radiation safety for Air Carrier Crewmembers. Rad Protect Dosim. 86(4):323-327.
52. Fujita T, Hüfner J. 1980. Momentum distributions after fragmentation in nucleus-nucleus collisions at high energy. Nucl Phys A. 343(2L):493-510.
53. Ganapol BD, Townsend LW, Wilson JW. 1989. Benchmark solutions for the galactic ion transport equations: energy and spatially dependent problems. Springfield (VA): National Technical Information Service. Report No.: NASA TP-2878.

54. Giacomelli M, Sihver L, Skvarč J, Yasuda N, Ilié R. 2004. Projectilelike fragment emission angles in fragmentation reactions of light heavy ions in the energy region < 200 MeV/nucleon: Modeling and simulations. Phys Rev C. 69(6):1-11.

55. Glauber RJ. 1955. Cross section in deuterium at high energies. Phys Rev. 100(1): 242-248.

56. Glauber RJ. 1959. High energy collision theory. In: Brittin WE, Dunham LG, editors. Lectures in theoretical physics. Volume 1. New York (NY): Wiley-Interscience, Inc.; c1959. p 315-414.

57. Glauber RJ, Matthiae G. 1970. High-energy scattering of protons by nuclei. Nucl Phys B. 21(1):135-157.

58. Gloeckler G, Jokipii JR. 1969. Physical basis of the transport and composition of cosmic rays in the galaxy. Phys Rev Lett. 22(26):1448-1453.

59. Goldberger M, Watson K. 1964. Collision Theory. New York (NY): Wiley-Interscience, Inc. 919 p.

60. Gosset J, Gutbrod HH, Meyer WG, Poskanzer AM, Sandoval A, Stock R, Westfall GD. 1977. Central collisions of relativistic heavy ions. Phys Rev C. 16(2):629-657.

61. Gunzert-Marx K, Iwase H, Schardt D, Simon RS. 2008. Secondary beam fragments produced by 200 MeV/u ^{12}C ions in water and their dose contributions in carbon ion radiotherapy. New J Phys. In press: March (2008).

62. Gutbrod HH, Sandoval A, Johansen PJ, Poskanzer AM, Gosset J, Meyer WG, Westfall GD, Stock R. 1976. Final-state interactions in the production of hydrogen and helium isotopes by relativistic heavy ions on uranium. Phys Rev Lett. 37(11):667-670.

63. Harrington DR. 1964. Double scattering corrections to high-energy diffraction scattering from deuterons. Phys Rev B. 135(2):358-364.

64. Harrington DR. 1969. Multiple scattering, the Glauber approximation, and the off-shell Eikonal approximation. Phys Rev. 184(5):1745-1749.

65. Haettner E, Iwase H, Schardt D. 2006. Experimental fragmentation studies with ^{12}C therapy beams. Rad Prot Dosimetry. 122(1-4):485-487.

66. Heilbronn LH. 2007. Personal communication.

67. Hüfner J, Schäfer K, Schürmann B. 1975. Abrasion-ablation in reactions between

relativistic heavy ions. Phys Rev C. 12(6):1888-1898.

68. Hüfner J. 1985. Heavy fragments produced in proton-nucleus and nucleus-nucleus collisions at relativistic energies. Phys Reports. 125(4):129-185.

69. Kerman AK, McManus H, Thaler RM. 1959. The scattering of fast nucleons from nuclei. Ann Phys. 8:551-635.

70. Kikuchi K, Kawai M. 1968. Nuclear matter and nuclear reactions. Amsterdam (Germany): North Holland Publishing. 336 p.

71. Lax M. 1951. Multiple scattering of waves. Rev Mod Phys. 23(4):287-310.

72. Lemaire MC, Nagamiya S, Schnetzer S, Steiner H, Tanihata I. 1979. Composite particle emission in relativistic heavy ion collisions. Phys Lett B. 85(1):38-42.

73. Madey R, Varga J, Baldwin AR, Anderson BD, Cecil RA, Fai G, Tandy PC, Watson JW. 1985. Inclusive neutron spectra at 0° from the reactions Pb(Ne,n)X and NaF(Ne,n)X at 390 and 790 MeV per nucleon. Phys Rev Lett. 55(14):1453-1456.

74. Madey R, Zhang WM, Anderson BD, Baldwin AR, Flanders BS, Pairsuwan W, Varga J, Watson JW. 1988. Inclusive neutron spectra at 0° from Nb-Nb and Au-Au collisions at 800 MeV/nucleon. Phys Rev C. 38(1):184-194.

75. Maung MK, Deutchman PA, Royalty WD. 1989. Integrals involving the three-parameter Fermi function. Can J Phys 67:95-99.

76. Miller TM. 2004. Comprehensive cross section database development for generalized three dimensional radiation transport codes. [Ph D. Dissertation]. Knoxville (TN): Nuclear Engineering department. University of Tennessee. 133 p.

77. Morrissey DJ, Marsh WR, Otto RJ, Loveland W, Seaborg GT. 1978. Target residue mass and charge distributions in relativistic heavy ion reactions. Phys Rev C. 18(3):1267-1274.

78. Morrissey DJ, Oliveira LF, Rasmussen JO, Seaborg GT, Yariv Y, Fraenkel Z. 1979. Microscopic and macroscopic model calculation of relativistic heavy-ion fragmentation reactions. Phys Rev Lett. 43(16):1139-1142.

79. Nagamiya S, Lemaire MC, Moeller E, Schnetzer S, Shapiro G, Steiner H, Tanihata I. 1981. Production of pions and light fragments at large angles in high-energy nuclear collisions. Phys Rev C. 24(3):971-1009.

80. Nakamura T, Heilbronn LH. 2006. Handbook on Secondary Particle Production and

Transport by High-Energy Heavy-Ions. New Jersey (NJ): World Scientific. 224.

81. [NAS/NRC] National Academy of Sciences/National Research Council (US). 1996. Radiation hazards to crews of interplanetary missions: biological issues and research strategies. Washington DC (NJ): National Academy Press (US).

82. Oliveira LF, Donangelo R, Ràsmussen JO. 1979. Abrasion-ablation calculations of large fragment yields from relativistic heavy ion reactions. Phys Rev C. 19(3):826-833.

83. Osborn TA. 1970. Glauber theory without the Eikonal approximation. Ann Phys. 58:417-453.

84. Papp J. 1975. Single Particle Inclusive Spectra Resulting from the Collision of Relativistic Protons, Deuterons, Alpha Particles, and Carbon Ions with Nuclei [Ph D. Dissertation]. Berkeley (CA): Lawrence Berkeley National Laboratory. Report No.: LBL-3633.

85. Pumplin J. 1968. Elastic scattering from deuterium. Phys Rev. 173(5):1651-1659.

86. Queen NM. 1964. Corrections to the impulse approximation for elastic nucleon-deuteron scattering. Nucl Phys. 55:177-196.

87. Remler EA. 1968. High-energy scattering by nuclei. Phys Rev. 176(5):2108-2112.

88. Rudstam G. 1966. Systematics of spallation yields. Z Naturforschung. 21A:1027-1041.

89. Sato H, Kurosawa T, Iwase H, Nakamura T, Uwamino Y, Nakao N. 2001. Measurements of double differential neutron production cross sections by 135 MeV/nucleon He, C, Ne and 95 MeV/nucleon Ar ions. Phys Rev C. 64(3):034607-1-12.

90. Schimmerling W. 1992. Radiological problems in space: an overview. Rad Env Biophys. 31:197-203.

91. Schwarzschild A, Zupančič Č. 1963. Production of tritons, deuterons, nucleons, and mesons by 30-Gev protons on Al, Be, and Fe targets. Phys Rev. 129(2):854-863.

92. Shinn JL, John S, Tripathi RK, Townsend LW, Norbury JW. 1992. Fully energy-dependent HZETRN (a galactic cosmic-ray transport code). Springfield (VA): National Technical Information Service. Report No.: NASA TP- 3243.

93. Simomsen LC, Nealy JE. 1991. Radiation protection for human missions to the

Moon and Mars. Springfield (VA): National Technical Information Service. Report No.: NASA TP- 3079.

94. Strapp HP, Ypsilantis TJ. 1957. Phase-shift analysis of 310-Mev proton-proton scattering experiments. Phys Rev. 105(1):302-310.

95. Townsend LW, Deutchman PA. 1981. Isobar giant resonance formation in self-conjugate nuclei. Nucl Phys. A355:505-532.

96. Townsend LW. 1983. Abrasion cross sections for ^{20}Ne projectiles at 2.1 GeV/nucleon. Can J Phys. 61:93-98.

97. Townsend LW, Wilson JW, Norbury JW, Bidasaria HB. 1984. An abrasion-ablation model description of galactic heavy-ion fragmentation. Springfield (VA): National Technical Information Service. Report No.: NASA TP-2305.

98. Townsend LW, Wilson JW, Norbury JW. 1985. A simplified optical model description of heavy ion fragmentation. Can J Phys. 63:135-138.

99. Townsend LW, Wilson JW, Cucinotta FA, Norbury JW. 1986. Comparison of abrasion model differences in heavy ion fragmentation: Optical versus geometric models. Phys Rev C. 34(4):1491-1494.

100. Townsend LW, Khan F, Tripathi RK. 1993. Optical model analyses of 1.65 GeV argon fragmentation cross sections and momentum distributions. Phys Rev C. 48(6):2912-2919.

101. Townsend LW. 1994. Optical model analyses of heavy ion fragmentation in hydrogen targets. Phys Rev C. 49(6):3158-3161.

102. Townsend LW, Cucinotta FA. 1996. Overview of nuclear fragmentation models and needs. Adv Space Res. 17(2):59-68.

103. Townsend LW. 2005. Implications of the space radiation environment for human exploration in deep space. Rad Protect Dosim. 115(1):44-50.

104. Tsao CH, Silberberg R, Barghouty AF, Sihver L, Kanai T. 1993. Scaling algorithm to calculate heavy-ion spallation cross sections. Phys Rev C. 47(3):1257-1262.

105. Watson KM. 1953. Multiple scattering and the many-body problem –applications to photomeson production in complex nuclei. Phys Rev. 89(3):575-587.

106. Weisskoph VF, Ewing DH. 1940. On the yield of nuclear reactions with heavy elements. Phys Rev. 57:472-485.

107. Westfall GD, Gosset J, Johansen PJ, Poskanzer AM, Meyer WG, Gutbrod HH, Sandoval A, Stock R. 1976. Nuclear fireball model for proton inclusive spectra from relativistic heavy-ion collisions. Phys Rev Lett. 37(18):1202-1205.
108. Wilkinson MC, Curtis SB. 1972. Galactic cosmic ray heavy primary secondary doses. Proceeding of the national symposium on natural and manmade radiation in space. Warman, EA. [ed]. Springfield (VA): National Technical Information Service. Report No.: NASA TM X-2440. p 104-107.
109. Wilson JW. 1974A. Proton-deuteron double scattering. Phys Rev C. 10(1):369-376.
110. Wilson JW. 1974B. Multiple scattering of heavy ions, Glauber theory, and optical model. Phys Lett B. 52(2):149-152.
111. Wilson JW, Costner CM. 1975. Nucleon and heavy-ion total and absorption cross section for selected nuclei. Springfield (VA): National Technical Information Service. Report No.: NASA TN-D-8107.
112. Wilson JW. 1977A. Analysis of the theory of high-energy ion transport. Springfield (VA): National Technical Information Service. Report No.: NASA TN-D-8381.
113. Wilson JW. 1977B. Depth-dose relations for heavy ion beams. Virginia J Sci. 28(3):136-138.
114. Wilson JW, Townsend LW. 1981. An optical model for composite nuclear scattering. Can J Phys. 59:1569-1576.
115. Wilson JW. 1983. Heavy ion transport in the straight ahead approximation. Springfield (VA): National Technical Information Service. Report No.: NASA TP-2178.
116. Wilson JW, Badavi FF. 1986. Methods of galactic heavy ion transport. Radiat Res. 108:231-237.
117. Wilson JW, Townsend LW, Badavi FF. 1987. A semiempirical nuclear fragmentation model. Nucl Inst Met Phys Res B. 18(3):225-231.
118. Wilson JW, Townsend LW. 1988. A benchmark for galactic cosmic-ray transport codes. Radiat Res. 114(2):201-206.
119. Wilson JW, Townsend LW, Schimmerling W, Khandelwal GS, Khan F, Nealy JE, Cucinotta FA, Norbury JW. 1991. Transport methods and interactions for space radiations. Springfield (VA): National Technical Information Service. Report No.:

NASA RP-1257.

120. Wilson JW, Shinn JL, Townsend LW, Tripathi RK, Badavi FF, Chun SY. 1994. NUCFRG2: a semiempirical nuclear fragmentation model. Nucl Inst Meth Phys Res B. 94:95-102.

121. Wilson JW, Cucinotta FA, Tai H, Simonsen LC, Shinn JL, Thibeault SA, Kim MY. 1997. Galactic and solar cosmic ray shielding in deep space. Springfield (VA): National Technical Information Service. Report No.: NASA TP-3682.

122. Wilson JW. 2000. Overview of radiation environments and human exposures. Health Phys. 79(5):470-494.

APPENDICES

APPENDIX A

APPENDIX A: optical limit approximation

The derivation in this appendix follows closely the original works by Braley et al. [11]; Townsend [94]; Watson [103]; Wilson [108]; and Wilson and Townsend [112]. Considering the multiple-scattering theory, the full Hamiltonian for the N nucleons system with two-body potentials is given by

$$H = \sum_{j} T_j + \sum_{i<j} V_{ij} + \sum_{\alpha} T_\alpha + \sum_{\beta<\alpha} V_{\beta\alpha} + \sum_{\alpha j} V_{\alpha j} \tag{A1}$$

where the Roman subscripts is the projectile, Greek subscripts is the target, T is the kinetic potential energy and V is the interaction potential [112]. The transition operator for scattering the α-constituent of the target with the *j*-constituent of the projectile is defined as

$$t_{\alpha j} = V_{\alpha j} + V_{\alpha j} G T_{\alpha j} \tag{A2}$$

where G is the complete non-interacting systems Green's function. The wave operator of the α and *j* collision is defined as

$$\omega_{\alpha j} = 1 + \sum_{(\beta,k)\neq(\alpha,j)} G t_{\beta k} \omega_{\beta k} \tag{A3}$$

where $\omega_{\alpha j}$ is the wave operator that transforms the system from the entering free state into the α and *j* collision state, and the second term in eq. (A3) represents the sum of the all wave operators including from the initial free state to the scattering states of other *β* and *k* constituents. The total wave operator becomes

$$\Omega = 1 + \sum_{\alpha j} G t_{\alpha j} \omega_{\alpha j} . \tag{A4}$$

Now considering the product of the relationship between the wave operator and the potential, the expression is given as

$$V_{\alpha j} \Omega = t_{\alpha j} \omega_{\alpha j} , \tag{A5}$$

The total transition operator *I* is then defined as the summation of the α and *j* constituents

$$I = \sum_{\alpha j} V_{\alpha j} \Omega = \sum_{\alpha j} t_{\alpha j} \omega_{\alpha j} . \tag{A6}$$

By iteration of eqs. (A3) and (A6), the multiple-scattering series for the exact scattering problem is expressed as

$$I = \sum_{\alpha j} t_{\alpha j} + \sum_{(\beta,k)\neq(\alpha,j)} t_{\alpha j} G t_{\beta k} + \ldots. \tag{A7}$$

The Green's function can be replaced by the free n-body Green's function, G_0, and then the problem becomes the two-body scattering problem. Next, the optical potential approximation is applied to the transition operator as

$$I = I_{opt} + \sum_{\alpha j} t_{\alpha j} G t_{\alpha j} + \ldots. \tag{A8}$$

and then applied the first order correction approximation as

$$I - I_{opt} \approx \frac{V_{opt} G V_{opt}}{A_P A_T}. \tag{A9}$$

where A_T and A_P are the atomic weights of the target and projectile, respectively.

Wilson [108] presented the expansion of the optical potential approximation from the usual Glauber optical limit model to correct the problem of convergence in the multiple-scattering series. The optical limit correlation effect is improved within the context of the eikonal scattering theory and appears to be accurate even for the light nuclei scattering. From the detailed derivation in Wilson and Costner [109], the optical potential expression is given as

$$W(x) = A_P A_T \int d^3 z\, \rho_T(z) \int d^3 y\, \rho_P(x+y+z)\, \bar{t}(e,y) \tag{A10}$$

where $\bar{t}$ is the average transition amplitude for two-body scattering

$$\bar{t} = \frac{1}{A_P A_T}\left[N_T N_P t_{nm} + Z_T Z_P t_{pp} + \left(Z_P N_T + Z_T N_P\right) t_{np}\right] \tag{A11}$$

and ρ_P and ρ_T are the projectile and target single particle number density distributions.

The probability of the collision is related to the optical potential of the profile function as

$$P^{A_P}(\mathbf{b},\mathbf{b}') = e^{i[\chi(\mathbf{b}) - \chi'(\mathbf{b}')} \tag{A12}$$

where the Eikonal phase shift function is

$$\chi(\mathbf{b}) = -\frac{A_P\, A_T}{2\pi\, k_{NN}} \int d^2 q\, e^{i\mathbf{q}\cdot\mathbf{b}} S_P(\mathbf{q})\, S_T(\mathbf{q})\, f_{NN}(\mathbf{q}) \tag{A13}$$

with $S(\mathbf{q})$ representing the one-body form factor and f_{NN} representing the two-body scattering amplitude as

$$f_{NN} = \frac{\sigma_{NN}(\alpha + i)\, k_{NN}}{4\pi} e^{-\frac{1}{2} B q^2} , \tag{A14}$$

to which the parameter σ_{NN} denotes the two-body total cross section, k_{NN} is the relative momentum in two-body center of mass frame, B is the two-body slope parameter, and α is the ratio of the real to imaginary part of f_{NN} ($\mathbf{q}$ = 0).

APPENDIX B

APPENDIX B.1: COAL subprogram

```
SUBROUTINE COAL(iat,iap,izt,izp,tnnlab,eel,plab,ne,dsunc,dxsd,dxst,dxsh,dxsa)
      IMPLICIT NONE
      REAL*8 pi,r0,sigma0,f,beta,delta,mu,amn,w,p0,tnnlab,gamma,eel(50),plab(50),
      dxsd(50),dxst(50),dxsh(50),dxsa(50),dxsum(50),dscoal(50),dsunc(50),
      cd(50),ct(50),ch(50),ca(50),tmp(50),deut_p0,trit_p0,helion_p0,alpha_p0
      INTEGER iat,iap,izt,izp,ad,zd,nd,at,zt,nt,ah,zh,nh,aa,za,na,ntar,nproj,ie,ne,i
      amn=939.57
      PI=4.*DATAN(1.D0)
      ntar=iat-izt
      nproj=iap-izp
      r0=1.26
c proton weitght factor is used for converting neutron xs to protons xs
      w=(real(izt+izp))/(real(ntar+nproj))
c sigma0 is a parameterized absorption cross section in two forms:
c the nucleon-nucleus form is due to Wilson et. al. 1988
c the nucleus-nucleus form is due to Townsend et. al. 1986
        IF ((iat.eq.1).or.(iap.eq.1)) THEN
          f=1-0.62*Exp(-tnnlab/200)*Sin(10.9*tnnlab**(-.28))
          IF (iat.eq.1) THEN
             sigma0=f*45.*real(iap)**.7*(1.+0.016*Sin(5.3-2.63*Log(real(iap))))
          else
            sigma0=f*45.*real(iat)**.7*(1.+0.016*Sin(5.3-2.63*Log(real(iat))))
          end if
          else
            beta=1.+5./tnnlab
            delta=0.2+1./real(iap)+1/real(iat)-0.292*Exp(-tnnlab/792.)*
                 Cos(0.229*tnnlab**0.453)
             mu=(real(iap)**(1./3.)+real(iat)**(1./3.)-delta)
```

```
          sigma0=10.*pi*(r0**2)*beta*(mu**2)
        END IF
c p0 is the coalescence radius for the resultant nuclei (MeV/c)
c these are approximations of those used in Gutbrod et. al
c     deut_p0=129
c     trit_p0=129
c     helion_p0=129 (observed production of helions is lt tritons)
c     alpha_p0=140
c these values are from Awes et. al. (1981); helion interpolated
c     deut_p0=170
c     trit_p0=215
c     helion_p0=240 (approx)
c     alpha_p0=270
c Nagamiya et. al. (1981) suggested p0 of ~90
    p0=90.0
    deut_p0=129
    trit_p0=129
    helion_p0=129
    alpha_p0=140
c Start looping to energies and values
c calculate proton invariant cross section from neutron invariant xs
c calculate Lorentz invariantxs for each fragment of interest
c set up dsunc as ddxs without coalescence effect
c Set up cases for each fragment of interest
c d=deuteron, t=triton, h=helion, a=alpha
    DO 70 i=1,ne
           plab(i)=((eel(i)**2)+(2*eel(i)*amn))**0.5
          tmp(i)=(eel(i)+amn)*sqrt((eel(i)**2)+(2*amn*eel(i)))
           zd=1
           nd=1
           ad=2
```

```
      cd(i)=((ad**2)/(zd*nd))*(w**zd)*((4.*pi*deut_p0**3./(3.*sigma0*
     &      amn*plab(i)*tmp(i)))**(ad-1)
      dxsd(i)=cd(i)*(dsunc(i)**ad)
      zt=1
      nt=2
      at=3
      ct(i)=((at**2)/(zt*nt))*(w**zt)*((4.*pi*trit_p0**3./(3.*sigma0*
     &      amn*plab(i)*tmp(i)))**(at-1)
      dxst(i)=ct(i)*(dsunc(i)**at)
      zh=2
      nh=1
      ah=3
      ch(i)=((ah**2)/(zh*nh))*(w**zh)*((4.*pi*helion_p0**3./(3.*sigma0*
     &      amn*plab(i)*tmp(i)))**(ah-1))
      dxsh(i)=ch(i)*(dsunc(i)**ah)
      za=2
      na=2
      aa=4
      ca(i)=((aa**2)/(za*na))*(w**za)*((4.*pi*alpha_p0**3./(3.*sigma0*
     &      amn*plab(i)*tmp(i)))**(aa-1))
      dxsa(i)=ca(i)*(dsunc(i)**aa)
      dxsum(i)=dxsd(i)+0.5*dxst(i)+dxsh(i)+0.5*dxsa(i)
      dscoal(i)=dsunc(i)-dxsum(i)
70    CONTINUE
      RETURN
      END
```

APPENDIX B.2: AMASS function

```
      FUNCTION AMASS(AIN,ZIN)
      IMPLICIT NONE
      REAL*8 ain,zin,x(300,0:120),am(58,0:30),amp,amn,a0,r0,pex,yex,amass,am0,
               ai,zi,av,as,ac,fk,xindex
      INTEGER nold,ia,iz,i,j,a,z
      CHARACTER(LEN=1) :: element,charge
     CHARACTER(LEN=10):: massnum

      DATA NOLD/0/
      IF(NOLD.GT.0)GO TO 1
      DATA AM/1798*0./
      DATA AV,AS,AC,FK/15.68,18.56,0.717,1.79/
      DATA AMP,AMN/938.6,939.57/
      A0=0.546
      R0=1.2049
      PEX=7.28897
      YEX=8.07132
      X(2,1)=13.135
      OPEN(unit=7,file='masstable1.dat',status='old',readonly)
      READ(7,*) element,charge,massnum
 90        READ(7,*,END=100)  i,j,xindex
           X(i,j) = xindex
           GOTO 90
100        CONTINUE
               DO 200 I=1,300
               DO 200 J=0,120
               IF(J.GT.I)  GO TO 200
               IF(X(I,J).eq.0)  X(I,J)=(I-J)*YEX+J*PEX
```

```
200 CONTINUE
      NOLD=1
  1  CONTINUE
            AM0=AIN*931.4
            IA=IFIX(SNGL(AIN))
            IZ=IFIX(SNGL(ZIN))
            IF(IZ.GT.IA)RETURN
            IF(IZ.LT.0) RETURN
          AMASS=AIN*931.4+X(IA,IZ)
    CLOSE (7)
    RETURN
    END
```

APPENDIX B.3: AWSPAR subprogram

```
SUBROUTINE AWSPAR(IAN,C,T)
implicit none
REAL*8 C,T
INTEGER ian

select case(ian)
case(4)
    t=0.327
    c=1.01
case(9)
    t=0.49
    c=2.35
case(12)
    t=0.49
    c=2.39
case(15)
    t=0.498
    c=2.334
case(16)
     t=.513
     c=2.608
case(19)
    t=0.564
    c=2.59
case(20)
    t=0.569
    c=2.47
```

```
…..………………
…………………..
…………………..
    case(209)
        t=0.56
        c=6.64
    case(238)
        t=0.606
        c=6.8054
    case default
         t=0.0
         c=0.0
    end select
    IF(C.EQ.0.AND.IAN.LT.40)C=3.4
    IF(T.EQ.0.AND.IAN.LT.40)T=0.54
    IF(C.EQ.0.AND.IAN.GT.40)C=0.0662*IAN+2.578
    IF(T.EQ.0.AND.IAN.GT.40)T=0.00005*IAN+0.556
    RETURN
    END
```

APPENDIX B.4: mass table database

A	Z	Mass(MeV)
1	0	8.071
1	1	7.289
2	1	13.136
3	1	14.95
3	2	14.93
4	1	26.0
4	2	2.425
4	3	25.32
5	1	38.49
5	2	11.39
5	3	11.68
6	1	41.86
6	2	17.59
6	3	14.09
6	4	18.37
7	2	26.11
7	3	14.91
7	4	15.77
7	5	27.87
8	2	31.6
8	3	20.95
8	4	4.94
8	5	22.92
8	6	35.1
9	2	40.82
9	3	24.95
9	4	11.35
9	5	12.42
9	6	28.91
10	3	33.44
10	4	12.61
10	5	12.05
10	6	15.7
10	7	39.7
11	3	40.79
11	4	20.17
11	5	8.67
11	6	10.65
11	7	24.96
12	4	25.07
12	5	13.37
12	6	0.0001
12	7	17.34
12	8	32.06
13	4	35.2
13	5	16.56
13	6	3.13
13	7	5.35
13	8	23.11
14	4	39.88
14	5	23.66
14	6	3.02
14	7	2.86
14	8	8.01
14	9	33.61
15	5	28.97
15	6	9.87
15	7	0.1
15	8	28.55
15	9	16.78
15	10	41.39
16	5	37.14
16	6	13.69
16	7	5.68
16	8	-4.74
16	9	10.68
16	10	23.99
17	5	43.72
17	6	21.04
17	7	7.87
17	8	-0.81
17	9	1.95
17	10	16.49
17	11	35.17
18	5	52.32
18	6	24.92
18	7	13.12
18	8	-0.78
18	9	0.87
18	10	5.32
18	11	25.32
19	5	59.36
19	6	32.83
19	7	15.86
19	8	3.33
19	9	-1.49
19	10	1.75
19	11	12.93
19	12	31.95
20	6	37.56
20	7	21.77
20	8	3.8
20	9	-0.02
20	10	-7.04
20	11	6.85
20	12	17.57
21	6	45.96
21	7	25.23
21	8	8.06
21	9	-0.05
21	10	-5.73
21	11	-2.18
21	12	10.91
21	13	26.12
22	6	52.58
22	7	32.08
22	8	9.28
22	9	2.79
22	10	-8.02
22	11	-5.18
22	12	-0.4
22	13	18.18
22	14	32.16
23	7	37.74
23	8	14.62
23	9	3.33
23	10	-5.15
23	11	-9.53
23	12	-5.47
23	13	6.77
23	14	23.77
24	7	47.04
24	8	18.97
24	9	7.54
24	10	-5.95
24	11	-8.42
24	12	-13.93
24	13	-0.06
24	14	10.76
24	15	32
25	8	27.14
25	9	11.27
25	10	-2.06
25	11	-9.36
25	12	-13.19
25	13	-8.91
25	14	3.83
25	15	18.87
26	8	35.16
26	9	18.29
26	10	0.43
26	11	-6.9
26	12	-16.21
26	13	-12.21
26	14	-7.14
26	15	10.97
26	16	25.97
27	9	25.05
27	10	7.09
27	11	-5.58
27	12	-14.59
27	13	-17.2
27	14	-12.39
27	15	-0.75
27	16	17.51
28	9	33.23
28	10	11.28
28	11	-1.03
28	12	-15.02
28	13	-16.85
28	14	-21.49
28	15	-7.16
28	16	4.07
28	17	26.56
29	9	40.3
29	10	18.02
29	11	2.62
29	12	-10.66
29	13	-18.22
29	14	-21.9
29	15	-16.95
29	16	-3.16
29	17	13.14
30	10	22.24
30	11	8.59
30	12	-8.88
30	13	-15.87
30	14	-24.43
30	15	-20.2
30	16	-14.06
30	17	4.4
30	18	20.08
31	10	30.84
31	11	12.66
31	12	-3.22
31	13	-14.95
31	14	-22.95
31	15	-24.44
31	16	-19.04
31	17	-7.06
31	18	11.3
32	10	37.18
32	11	18.3
32	12	-0.8
32	13	-11.06
32	14	-24.08
32	15	-24.31
32	16	-26.02
32	17	-13.33
32	18	-2.18
32	19	20.42
33	11	25.51
33	12	5.2

234	91	40.34
234	92	38.14
234	93	39.95
234	94	40.34
234	95	44.51
235	90	44.25
235	91	42.32
235	92	40.91
235	93	41.04
235	94	42.2
235	95	44.74
235	96	48.05
236	91	45.34
236	92	42.44
236	93	43.38
236	94	42.89
236	95	46.17
236	96	47.88
237	91	47.64
237	92	45.38
237	93	44.87
237	94	45.09
237	95	46.82
237	96	49.27
237	97	53.21
238	91	50.76
238	92	47.3
238	93	47.45
238	94	46.16
238	95	48.42
238	96	49.38
238	97	54.34
239	92	50.57
239	93	49.3
239	94	48.58
239	95	49.38
239	96	51.09
239	97	54.36
239	98	58.28
240	92	52.71
240	93	52.32
240	94	50.12
240	95	51.5
240	96	51.71
240	97	55.66
240	98	58.03
241	93	54.26
241	94	52.95
241	95	52.93
241	96	53.7
241	97	56.1
241	98	59.35
241	99	63.9
242	93	57.41
242	94	54.71
242	95	55.46
242	96	54.8
242	97	57.8
242	98	59.33
242	99	64.94
243	93	59.92
243	94	57.75
243	95	57.17
243	96	57.18
243	97	58.68
243	98	60.9
243	99	64.86
243	100	69.4
244	94	59.8
244	95	59.87
244	96	58.45
244	97	60.7
244	98	61.47
244	99	66.03
244	100	69.05
245	94	63.1
245	95	61.89
245	96	61.0
245	97	61.81
245	98	63.38
245	99	66.43
245	100	70.21
246	94	65.39
246	95	64.99
246	96	62.61
246	97	63.96
246	98	64.08
246	99	67.97
246	100	70.12
247	95	67.23
247	96	65.53
247	97	65.48
247	98	66.13
247	99	68.6
247	100	71.52
247	101	76.1
248	95	70.49
248	96	67.38
248	97	68.1
248	98	67.23
248	99	70.29
248	100	71.89
248	101	77.15
249	96	70.74
249	97	69.84
249	98	69.72
249	99	71.17
249	100	73.61
249	101	77.32
250	96	72.98
250	97	72.94
250	98	71.16
250	99	73.27
250	100	74.07
250	101	78.7
251	96	76.64
251	97	75.22
251	98	74.13
251	99	74.5
251	100	75.98
251	101	79.05
251	102	82.83
252	97	78.53
252	98	76.03
252	99	77.29
252	100	76.81
252	101	80.7
252	102	82.87
253	97	80.8
253	98	79.29
253	99	79.01
253	100	79.34
253	101	81.3
253	102	84.48
253	103	88.73
254	98	81.33
254	99	81.99
254	100	80.9
254	101	83.58
254	102	84.72
254	103	89.87
255	98	84.78
255	99	84.08
255	100	83.79
255	101	84.83
255	102	86.85
255	103	90.09
255	104	94.55
256	99	87.15
256	100	85.48
256	101	87.61
256	102	87.82
256	103	92.01
256	104	94.25
257	99	89.4
257	100	88.58
257	101	88.99
257	102	90.22
257	103	92.73
257	104	96.15
257	105	100.46
258	100	90.46
258	101	91.68
258	102	91.52
258	103	94.91
258	104	96.39
258	105	101.84
259	100	93.7
259	101	93.62
259	102	94.12
259	103	95.93
259	104	98.38
259	105	102.2
259	106	106.85
260	101	96.6
260	102	95.6
260	103	98.34
260	104	99.24
260	105	103.8
260	106	106.6
261	101	98.4
261	102	98.5
261	103	99.62
261	104	101.45
261	105	104.43
261	106	108.38
261	107	113.45
262	102	100.2
262	103	102.3
262	104	102.55
262	105	106.54
262	106	108.6
262	107	114.68
263	102	103.2
263	103	103.77
263	104	105.0
263	105	107.39
263	106	110.5
263	107	114.86
264	103	106.5
264	104	106.3
264	105	109.63
264	106	111.11
264	107	116.35
264	108	119.82
265	103	108.2
265	104	108.8
265	105	110.7
265	106	113.11
265	107	116.82
265	108	121.63
266	104	110.4
266	105	112.99
266	106	114.03
266	107	118.72
266	108	121.7
266	109	128.39

APPENDIX C

APPENDIX C.1: Secondary neutron sample results

C.1.1. 95 MeV/nucleon ^{40}Ar + ^{207}Pb collisions

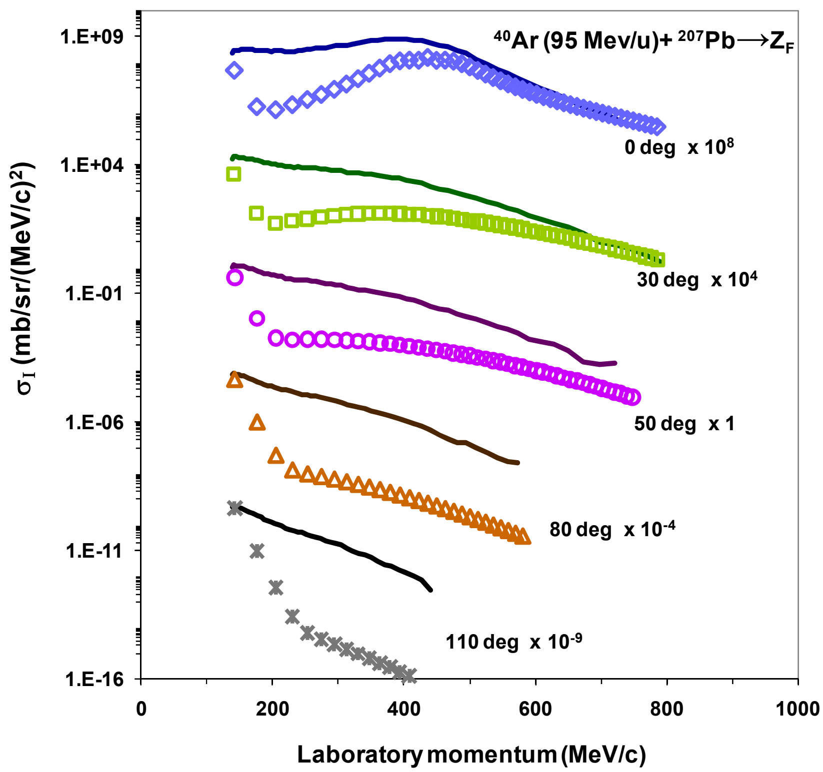

Figure C.1.1: Distributions of Lorentz invariant cross sections of total secondary neutron at various laboratory angles for 95 MeV/nucleon ^{40}Ar + ^{207}Pb reactions. Line plots represent the experimental data and symbols represent the calculations from the ABRKO and INQE subprograms after separating the contributions of projectile and target. For display purposes, both measurements [79] and calculations are multiplied by multiplication factors of $10^{-9} - 10^{8}$.

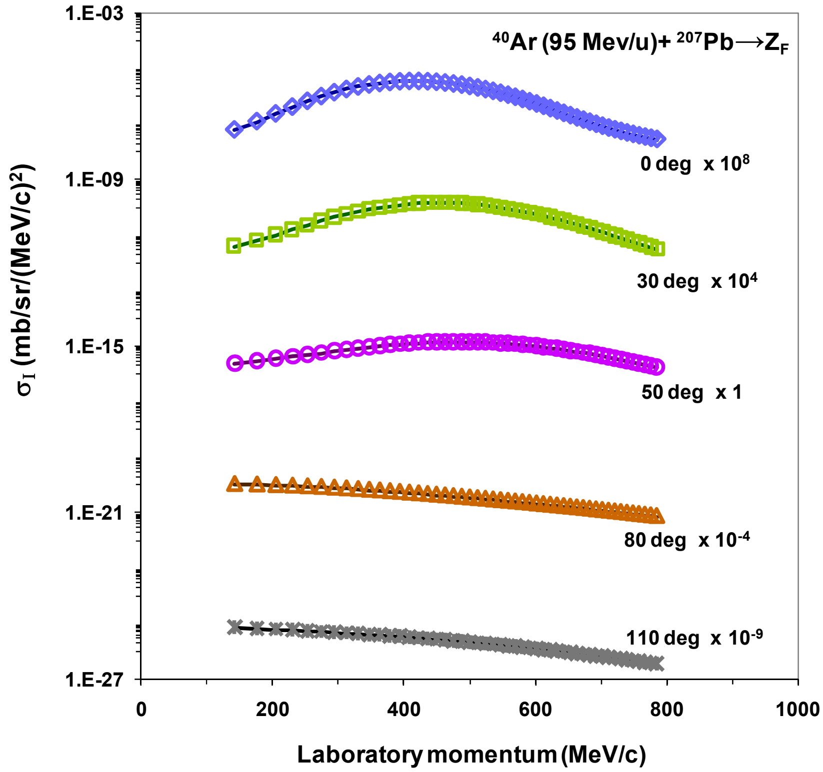

Figure C.1.2: Distributions of Lorentz invariant cross sections of abraded secondary neutron from contributions of projectile at various laboratory angles for 95 MeV/nucleon $^{40}Ar + ^{207}Pb$ reactions. Line plots represent the calculations from the ABRKO and INQE subprograms before separating the contributions of projectile and target and symbols represent the calculations after separating the contributions of projectile and target. For display purposes, both calculations are multiplied by multiplication factors of $10^{-9} – 10^{8}$.

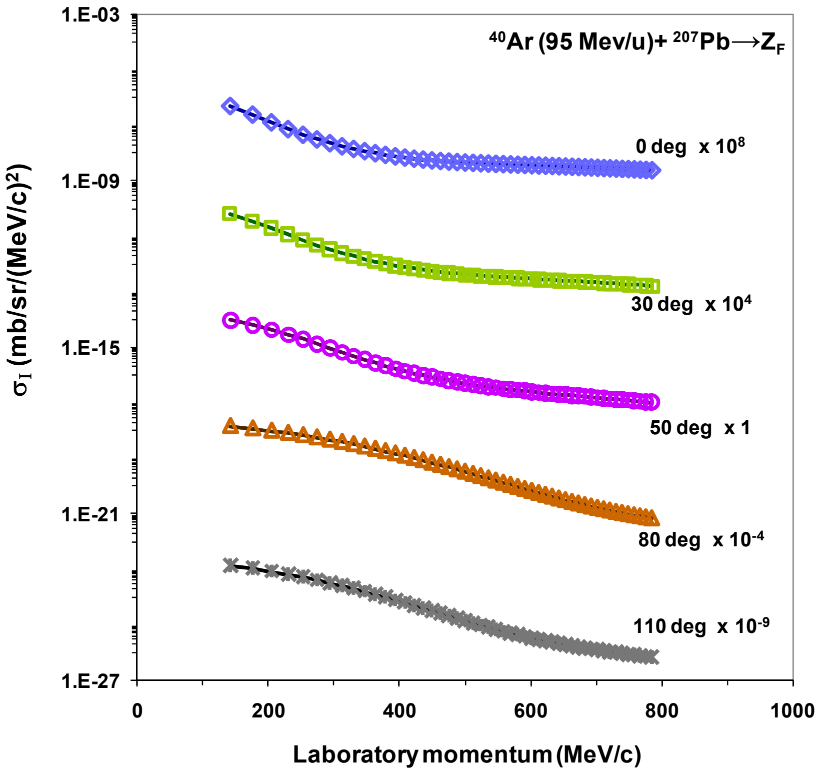

Figure C.1.3: Distributions of Lorentz invariant cross sections of abraded secondary neutron from contributions of target at various laboratory angles for 95 MeV/nucleon $^{40}Ar + ^{207}Pb$ reactions. Line plots represent the calculations from the ABRKO and INQE subprograms before separating the contributions of projectile and target and symbols represent the calculations after separating the contributions of projectile and target. For display purposes, both calculations are multiplied by multiplication factors of $10^{-9} – 10^{8}$.

C.1.2. 400 MeV/nucleon $^{40}Ar + {}^{12}C$ collisions

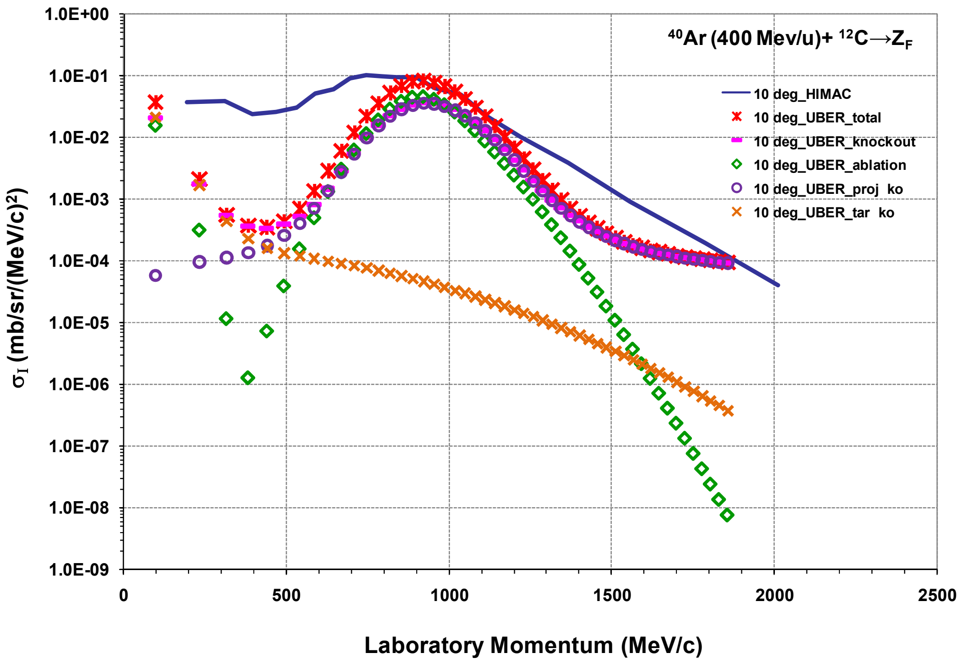

Figure C.1.4: Lorentz invariant neutron cross sections of 400 MeV/nucleon ^{40}Ar colliding with ^{12}C target at 10º laboratory forward angle from both measurements and calculations. Separate contributions from the knockout stage (dash lines), the ablation stage (diamonds), and their sums (asterisks) are indicated for the calculations. The contributions of projectile (open circles) and target (cross symbols) from knockout processes are also explicitly displayed for the calculated results. The experimental data are reported in [79].

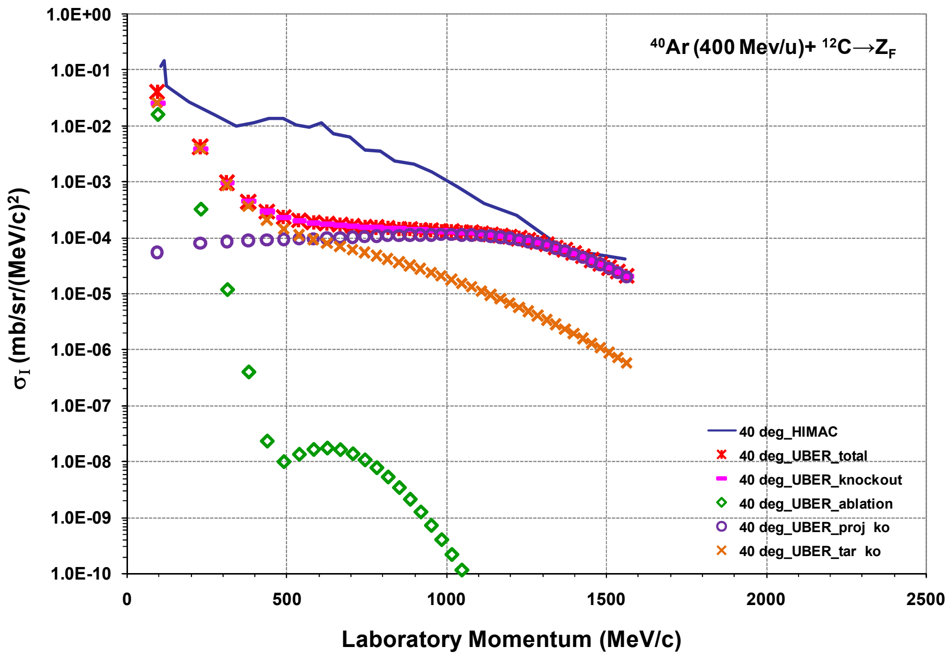

Figure C.1.5: Lorentz invariant neutron cross sections of 400 MeV/nucleon ^{40}Ar colliding with ^{12}C target at 40º laboratory forward angle from both measurements and calculations. Separate contributions from the knockout stage (dash lines), the ablation stage (diamonds), and their sums (asterisks) are indicated for the calculations. The contributions of projectile (open circles) and target (cross symbols) from knockout processes are also explicitly displayed for the calculated results. The experimental data are reported in [79].

C.1.3. 337 MeV/nucleon ^{20}Ne + ^{238}U collisions

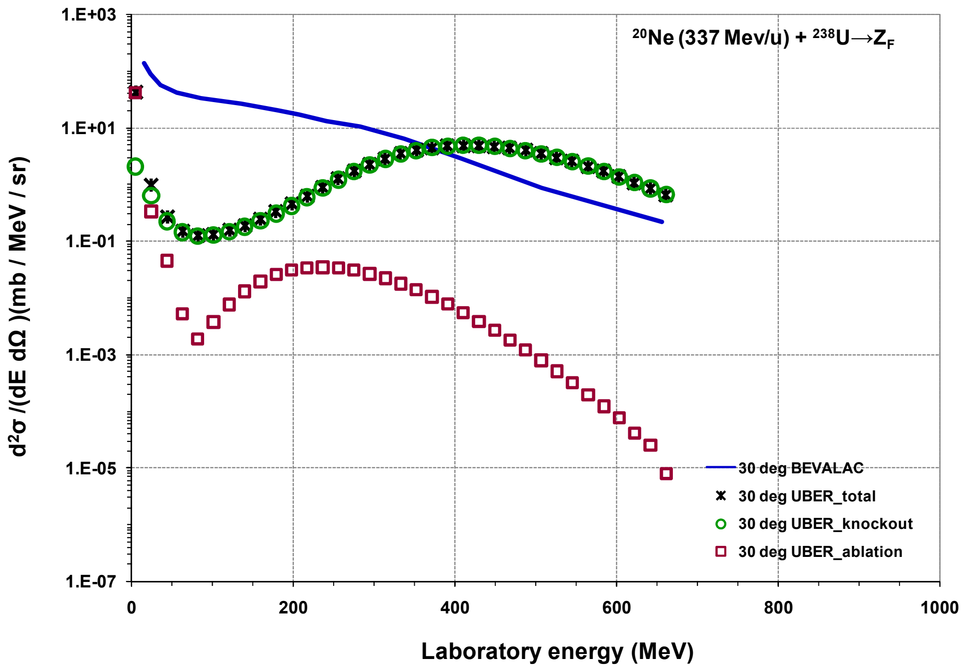

Figure C.1.6: Secondary neutron spectral distribution displayed as double differential cross sections for the reaction of 337 MeV/nucleon ^{20}Ne colliding with a ^{238}U target at 30^{o} laboratory angle compared with published measured data [79] as shown in the solid line. Separate contributions from knockout stage (dash lines), ablation stage (diamonds), and their sums (asterisks) for the calculations are also displayed. The contributions of projectile (open circles) and target (plus symbols) from the knockout process are also explicitly displayed for the calculated results.

VITA

Sirikul Sriprisan was born in Bangkok, Thailand. She came to the United States of America after she graduated from Sai Num Phueng High School in Bangkok. She received her Master's degree in BioEngineering from Oregon State University in 2002, then worked as a network/operating system analyst in the BioEngineering Department, Oregon State University, Corvallis, Oregon. In 2003, she joined the Nuclear Engineering Department, Oregon State University, for studies in the doctoral program. In the summer 2004, she attended the internship program at the Oak Ridge National Laboratory where she worked on the research projects in the Nuclear Science and Technology Division; she was under a supervision of Bernadette Kirk and Ian Gauld. Her first project involved dose calculations for Brachytherapy cancer treatments using deterministic methods. She implemented nuclear modeling computational codes such as TORT, DORT, XSDRN and NJOY99. The second project she involved in was related to the analysis of worldwide spent fuel inventories using the ORIGEN spent fuel analysis code. The codes she implemented included ORIGEN, MCNP, and some SCALE packages. In January of 2005, she began her pursuit of the doctoral degree in the Nuclear Engineering at the University of Tennessee, Knoxville, which she completed in July 2008. Her dissertation work was sponsored by the National Aeronautics and Space Administration. During this course of study, she had attended MCNPX5.0 training in West Point, New York and the FLUKA training in Houston, Texas. After the completion of her degrees, she will work as a postdoctoral researcher in the Nuclear Engineering Department at the University of Tennessee.